STAR Analysis Note: psn0689
Analysis Note for Hyperon Transverse Spin Transfer with run12 data

Jincheng Mei, Qinghua Xu

June 12, 2018

Contents

1 Introduction **7**

2 Data Set **9**
2.1 Trigger selection 9
2.2 Beam polarization 11
2.3 Relative luminosity 11

3 $\Lambda\,(\bar{\Lambda})$ Reconstruction and Jet Correlation **13**
3.1 $\Lambda\,(\bar{\Lambda})$ Reconstruction 13
3.2 Jet Correlation 16
3.3 Control sample: K^0_S 17

4 Extraction of Transverse Spin Transfer **26**
4.1 Trigger Combined $D_{\rm TT}$ 30
4.2 Cross check of $D_{\rm TT}$ measurement method 35

5 MC Production and Data Comparison **37**
5.1 MC Production 37
5.2 Data and MC Comparison 37

6 Evaluation of Systematic Uncertainty **47**
6.1 Uncertainty from Decay parameter 47
6.2 Uncertainty from Beam polariaztion 47
6.3 Uncertainty from Estimation of Residual Background Fraction 47
6.4 Uncertainty from Pileup 48
6.5 Uncertainty from Trigger Bias 50
6.6 Total Systematic Uncertainty 59

7 Final Results **62**

8 Main Code **64**
8.1 Data Analysis: from MuDsts to D_{TT} 64
8.2 MC production 66
8.3 Notes 66

A Run List **68**

List of Figures

1.1 Depolarization $D_{\rm NN}$ data as a function of $p_{\rm T}$ in $p^{\uparrow} + p \to \Lambda^0 + X$ at 200 GeV/c from Fermilab E704 Collaboration measurement. The errors shown are statistical only. 7
2.1 z of primary vertex for each of the JP trigger samples 10
2.2 z of primary vertex combined four JP trigger samples 11
2.3 Relative luminosities calculated using the Jet-Patch events without Λ or $\bar{\Lambda}$ candidates. They are used to form the single spin collision events. . . . 12
3.1 Sketch of topological cuts applied in the reconstruction of Λ and $\bar{\Lambda}$. 14
3.2 Invariant mass distributions of Λ and $\bar{\Lambda}$ candidates after topological selections for the trigger-combined sample. 15
3.3 $p_{\rm T}$ distribution of reconstructed jets. 16
3.4 η distribution of reconstructed jets. 17
3.5 ϕ distribution of reconstructed Jets. 19
3.6 ΔR distribution in the correlation between the reconstructed jet and $\Lambda\,(\bar{\Lambda})$ from JP1 trigger sample as the example. 20
3.7 The invariant mass distributions of jet near-side Λ and $\bar{\Lambda}$ candidates for the trigger-combined samples. 21
3.8 The $p_{\rm T}$ distributions of Λ and $\bar{\Lambda}$ candidates in the jet near-side from the four JP trigger samples. 22
3.9 The η distributions of Λ and $\bar{\Lambda}$ candidates in the jet near-side from the four JP trigger samples. 23
3.10 The ϕ distributions of Λ and $\bar{\Lambda}$ candidates in the jet near-side from the four JP trigger samples. 24
3.11 Invariant mass of K^0_S candidates for the trigger-combined sample. 25
4.1 Symmetry test of Λ counts when both of the beam polarization and $\cos\theta^*$ reverse. 27
4.2 Symmetry test of $\bar{\Lambda}$ counts when both of the beam polarization and $\cos\theta^*$ reverse. 28
4.3 Average values of relative luminosities over runs. 29
4.4 $\cos\theta^*$ vs. invariant mass distribution for Λ(left) and $\bar{\Lambda}$(right) with $2 < p_{\rm T} < 3$ GeV/c and $0 < \eta < 1.2$from JP1 sample with the BLUE beam as the polarized beam. 30
4.5 $\cos\theta^*$ distribution for (a) Λ and (b) $\bar{\Lambda}$ from JP1 sample. The solid circle denotes the positive beam polarization and the open circle denotes the negative beam polarization. 31
4.6 $D_{\rm TT}$ vs. $\cos\theta^*$ for Λ(left) and $\bar{\Lambda}$(right) with $p_{\rm T}$ of $2 \sim 3$ GeV/c using JP1 data. 31
4.7 $D_{\rm TT}$ for the 4 JP trigger samples. The upper panel is for Λ and the lower is for $\bar{\Lambda}$. The η range is $0 \sim 1.2$ in the left and $-1.2 \sim 0$ in the right. . . . 32
4.8 $D_{\rm TT}$ for $\Lambda\,(\bar{\Lambda})$ and $\delta_{\rm TT}$ for K^0_S vs. $\cos\theta^*$ in each $p_{\rm T}$ bin from the trigger-combined data sample. 33

4.8 D_{TT} for $\Lambda\,(\bar{\Lambda})$ and δ_{TT} for K^0_S vs. $\cos\theta^*$ in each p_{T} bin from the trigger-combined data sample. 34
4.9 D_{TT} for the trigger-combined sample. The left and right plots are for $0 < \eta < 1.2$ and $-1.2 < \eta < 0$, correspondingly. 35
4.10 The comparison between the results extracted via Cross-Ratio method and Relative Luminosity method. The left and right plots are for $0 < \eta < 1.2$ and $-1.2 < \eta < 0$, correspondingly. 36
4.11 The comparison between the results extracted by using the hyperon aixs and the jet axis as the substitute of the quark axis, separately. 36
5.1 Hard Hard p_{T} distributions before (left) and affter (right) weighting for each of Λ p_{T} bins. 38
5.1 Hard p_{T} distribution before (left) and affter (right) weighting for each of Λ p_{T} bins. 39
5.2 Comparison of primary vertex z after reweighting. The plots are for JP0, JP1, JP2, AJP trigger conditions from left to right in sequence. 40
5.3 Comparison of reconstrcuted variables of $p\,(\bar{p})$ from jet near-side $\Lambda\,(\bar{\Lambda})$. The invariant mass of $\bar{\Lambda}$ are shown in the left panel and the right one is for Λ. 41
5.4 Comparison of reconstrcuted variables for jet near-side Λ and $\bar{\Lambda}$. The p_{T}, η, ϕ comparisons for Λ are shown in the upper panel and the lower panel is for $\bar{\Lambda}$. 41
5.5 Comparisons of reconstrcuted variables of $p\,(\bar{p})$ from jet near-side $\Lambda\,(\bar{\Lambda})$. The p_{T}, η, ϕ comparisons for p from Λ are shown in the upper panel and the lower panel is for $\bar{p}$ from $\bar{\Lambda}$. 42
5.6 Comparisons of reconstrcuted variables for π^- (π^+) decay from jet near-side $\Lambda\,(\bar{\Lambda})$. The p_{T}, η, ϕ comparisons for π^- from Λ are shown in the upper panel and the lower panel is for π^+ from $\bar{\Lambda}$. 43
5.7 Comparisons of selection cuts for jet near-side Λ and $\bar{\Lambda}$. The decay length, DCA_V0, DCA_2 comparisons for Λ are shown in the upper panel and the lower panel is for $\bar{\Lambda}$. 44
5.8 DCA of p, π from jet near-side Λ and $\bar{\Lambda}$. The upper panel is for Λ and the lower panel is for $\bar{\Lambda}$. 45
5.9 The ratio of $\bar{\Lambda}/\Lambda$ yield in different states. The left plot is for inclusive Λ and $\bar{\Lambda}$ and the right one is for the jet near-side Λ and $\bar{\Lambda}$. 46
6.1 Hyperon yield vs. collision rate in spin 4-bit configurations of Λ for JP trigger combination. The upper-left graph is for spinbit-5, the upper right graph is for spinbit-6, the low left one is for spinbit-9 and the low right one is for spinbit-10. 49
6.2 Hyperon yield vs. collision rate in spin 4-bit configurations of $\bar{\Lambda}$ for JP trigger combination. The upper-left graph is for spinbit-5, the upper right graph is for spinbit-6, the low left one is for spinbit-9 and the low right one is for spinbit-10. 49

6.3 z distribution for Λ (in the left) and $\bar{\Lambda}$ (in the right) with p_{T} of $3 \sim 4\,\mathrm{GeV}/c$. X aixs shows z and Y axis shows the yield after normalized. The shifts of the mean values related to the mean value of zero bias sample are shown in the legend. 51
6.4 D_{TT} for Λ and $\bar{\Lambda}$ versus z calculated using the model in different p_{T} bins with positive η (left) and negative η (right). 52
6.4 D_{TT} for Λ and $\bar{\Lambda}$ versus z calculated using the model in different p_{T} bins with positive η (left) and negative η (right). 53
6.5 The relative fractions of subprocess for Λ (upper panel) and $\bar{\Lambda}$ (lower panel) with p_{T} of $3 \sim 4\,\mathrm{GeV/c}$. 55
6.6 The relative fractions of subprocess for Λ (upper panel) and $\bar{\Lambda}$ (lower panel) in all p_{T} bins. 56
6.7 The relative fractions of fragmenting parton flavors for Λ (upper panel) and $\bar{\Lambda}$ (lower panel) with p_{T} of $3 \sim 4\,\mathrm{GeV/c}$. 57
6.8 The relative fractions of fragmentin parton flavors for Λ (upper panel) and $\bar{\Lambda}$ (lower panel) in all p_{T} bins. 58
6.9 The feed-down fractions for Λ (upper panel) and $\bar{\Lambda}$ (lower panel) in all p_{T} bins. 60
7.1 D_{TT} extracted from the trigger combined sample for Λ and $\bar{\Lambda}$. The left grpah is with positive η with respect to the polarized beam and the right one is with negative η with respect to the polarized beam. 63

List of Tables

2.1 Ratio of the overlap events between each two triggers. The ratio is the number of events belonging to the trigger of the column and the one of the row together over the number of events belonging to the trigger of the column. 10
3.1 Summary of selection cuts for $\Lambda\,(\bar{\Lambda})$ reconstruction for Jet-Patch trigger data sample. Here "DCA" denotes "distance of closest approach", "PV" denotes "primary vertex", $\vec{r}$ denotes the vector from primary vertex to the V0 vertex and $\vec{p}$ denotes the momentum vector of V0. Fig. 3.1 shows definitions of topological selection cuts as a reference. 13
3.2 Λ and $\bar{\Lambda}$ candidate counts, residual background fractions and signal mass windows after topological selection. 14
3.3 Jet near-side Λ and $\bar{\Lambda}$ candidate counts, residual background fractions and signal mass windows. 18
3.4 The fraction of hyperons falling in the jet near-side cone for Λ and $\bar{\Lambda}$ in each p_{T} bin. 18
3.5 Summary of selection cuts for K^0_S reconstruction for Jet-Patch trigger data sample. Here "DCA" denotes "distance of closest approach", "PV" denotes "primary vertex", $\vec{r}$ denotes the vector from primary vertex to the V0 vertex and $\vec{p}$ denotes the momentum vector of V0. Fig. 3.1 shows definitions of topological selection cuts as a reference. 25
4.1 χ^2/ndf testing between the results of each two trigger samples 31
6.1 Uncertainty to D_{TT} from estimation of residual background fraction for Λ and $\bar{\Lambda}$ 48
6.2 Factors of pileup contribution for Λ and $\bar{\Lambda}$ for each spin configuration. . . 48
6.3 Uncertainty to D_{TT} from pileup for Λ and $\bar{\Lambda}$ 50
6.4 Uncertainty to D_{TT} from z shift for Λ and $\bar{\Lambda}$ 53
6.5 Uncertainty to D_{TT} from subprocess & fragmenting parton flavor for Λ and $\bar{\Lambda}$ 59
6.6 Uncertainty to D_{TT} from feed-down for Λ and $\bar{\Lambda}$ 61
6.7 Total Systematic Uncertainty 61
7.1 Values of D_{TT} extracted form trigger combined sample 62

1 Introduction

The spin structure of the proton is a hot topic in QCD. After many years' studies on the longitudinal spin structure, rich knowledge about it has been obtained but the transverse spin structure is still poorly known. Λ and other hyperons have been studied extensively in different aspects of spin physics, due to their self-analyzing weak decay.

In 1997, a significant spin transfer along the normal direction of the Λ production plane, $D_{\rm NN}$, was observed by the E704 Collaboration at Fermilab [2].

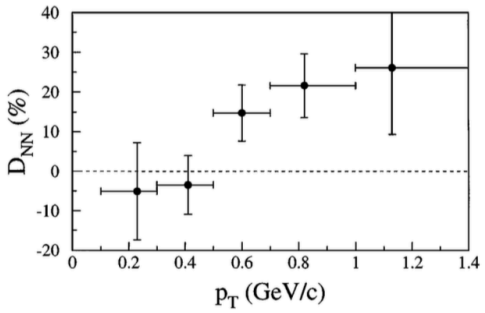

Figure 1.1: Depolarization $D_{\rm NN}$ data as a function of $p_{\rm T}$ in $p^{\uparrow}+p \to \Lambda^0+X$ at 200 GeV/c from Fermilab E704 Collaboration measurement. The errors shown are statistical only.

The transverse spin transfer, $D_{\rm TT}$, of hyperons in pp collisions is defined in Eq. 1.1 as the asymmetry of the cross section of hyperons polarized parallel and anti-parallel to the incoming protons. It is the natural connection to the transversely polarized parton distribution and the transversely polarized fragmentation functions.

$$D_{\rm TT}^{\Lambda} \equiv \frac{d\sigma^{(p^{\uparrow}p\to\Lambda^{\uparrow}X)} - d\sigma^{(p^{\uparrow}p\to\Lambda^{\downarrow}X)}}{d\sigma^{(p^{\uparrow}p\to\Lambda^{\uparrow}X)} + d\sigma^{(p^{\uparrow}p\to\Lambda^{\downarrow}X)}} = \frac{d\delta\sigma^{\Lambda}}{d\sigma^{\Lambda}}, \tag{1.1}$$

where $\uparrow$ and $\downarrow$ denote the positive and negative polarization directions correspondingly, $\delta\sigma^{\Lambda}$ is the cross section of Λ when the initial state is transversely polaried and σ^{Λ} is the cross section of Λ when the initial state is unpolarized. $\delta\sigma^{\Lambda}$ can be factorized into three parts shown as 1.2 [8]:

$$\frac{d\delta\sigma^{\Lambda}}{dp_{\rm T}^{\Lambda}} = \sum_{abcd} \int dx_a dx_b dz \delta f_a(x_a) f_b(x_b) \delta\sigma^{(a^{\uparrow}b\to c^{\uparrow}d)} \delta D_c^{\Lambda}(z), \tag{1.2}$$

where, $\delta D_c^H(z)$ and $\delta f(x)$ are the polarized fragmentation function in the transversely polarized case and the transversity distribution function of the quarks or antiquarks. They can be studied experimentally in semi-inclusive deep inelasitic lepton-nucleon scattering with transversely polarized nucleon or high$-p_{\rm T}$ hyperon production in transvesely polarized pp collisions by measuring the hyperon polarization in the final state. The partonic spin transfer factor for the elementary hard scattering process is denoted by $\delta\sigma^{(a^{\uparrow}b\to c^{\uparrow}d)}$, which is calculatable by pQCD [3].

We present the first measurement on transverse spin transfer of Λ and $\bar{\Lambda}$ in transversely polarized pp collisions at $\sqrt{s} = 200\,\mathrm{GeV}$ with the STAR detector at RHIC. The measurement covers a kinematic range of $|\eta| < 1.2$ in pseudo-rapidity and transverse momentum p_T from $1.0\,\mathrm{GeV/c}$ up to $8.0\,\mathrm{GeV/c}$. The spin transfer, D_TT, is determined from the asymmetry of Λ counts with opposite beam polarization states, in which the detector acceptance mostly cancels. D_TT dependent on p_T is presented both in positive and negative pseudo-rapidity ranges.

2 Data Set

2.1 Trigger selection

The data used in this analysis is the transversely polarized pp collisions taken in 2012 at $\sqrt{s} = 200\,\text{GeV}$ with STAR detector and was produced with library P12id. Four triggers are selected in the analysis:

- Jet-Patch 0 (JP0) trigger with id 370601.
- Jet-Patch 1 (JP1) trigger with id 370611.
- Jet-Patch 2 (JP2) trigger with id 370621.
- Adjacent Jet Patch (AJP) trigger with id 370641.

QA was applied for Jet-Patches samples for hyperon analysis and 573 runs left. The average values of some variables per event in each run are used to test the data quality. For each variable, the average value should be stable or have a regularity with the fill running. The run is removed if it is strongly deviated from the average line or regularity. The QA details can be found at:
`http://www.star.bnl.gov/protected/spin/jcmei/pp200trans_2012/htmlCode/pp200trans_2012_dataQA.html`
The short runs whose running time is shorter than 3 mins or events are smaller than 5k are also removed. Considering that we need to make the correlation between Λ hyperons and reconstructed jets, the runs removed in J. Kevin Adkins' jet tree are also removed. The run number list can be found in Appendix.

The events with primary vertex of $|V_z| < 60\,\text{cm}$ are selected to ensure uniform tracking efficiency.

The Jet-Patch (JP) trigger conditions in 2012 required a transvese energy deposit in a patch of towers of BEMC or EEMC to exceed the threshold. The BEMC or EEMC patch covers $\Delta\eta \times \Delta\phi = 1 \times 1$ in pseudo-rapidity, η and azimuthal angle, ϕ. The thresholds are $E_\text{T} \sim 3.5\,\text{GeV}$ for JP0, $E_\text{T} \sim 5.4\,\text{GeV}$ for JP1, $E_\text{T} \sim 7.3\,\text{GeV}$ for JP2 and two adjacent patches to ecah exceed $E_\text{T} \sim 3.5\,\text{GeV}$ for AJP. JP triggers are preferred to collecting pp events including scaterring with high transverse momentum transfer. Consequently, the p_T of Λ ($\bar{\Lambda}$) produced through the fragmentation of high transverse momentum parton is expected to be higher. However, JP triggers are not (necessarily) caused by Λ or $\bar{\Lambda}$. This implies that the trigger is biased in a way that is different for different classes of Λ or $\bar{\Lambda}$. The trigger bias effect on our measurement is considered as a systematic uncertainty and will be disscused in Section 6.

The overlap events were only taken into one (the one with lower threshold) of the fired triggers to avoid double counting. The ratio of the overlap events between each two triggers are shown in TABLE 2.1

The statistics of the data sample used in this analysis are 141.7 M totally and for each trigger sample used are:

- 24.6 M JP0 events.

- 85.3 M JP1 events.
- 18.0 M JP2 events.
- 13.9 M AJP events.

The distributions of primary vertex z for each of the JP trigger samples are shown in Fig. 2.1. The distribution of primary vertex z for trigger-combined sample is shown in Fig. 2.2.

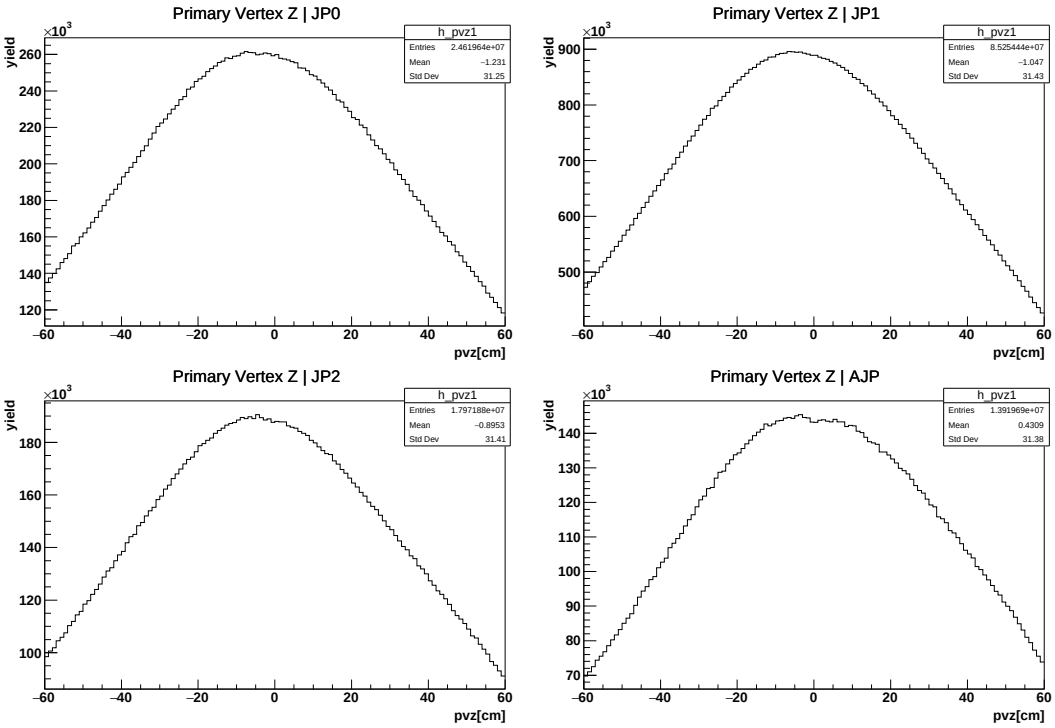

Figure 2.1: z of primary vertex for each of the JP trigger samples

Table 2.1: Ratio of the overlap events between each two triggers. The ratio is the number of events belonging to the trigger of the column and the one of the row together over the number of events belonging to the trigger of the column.

Trigger Overlap	JP0	JP1	JP2	AJP
JP0	100.00%	1.01%	0.86%	0.85%
JP1	8.64%	100.00%	42.19%	14.53%
JP2	2.97%	16.89%	100.00%	8.40%
AJP	1.33%	2.66%	3.84%	100.00%

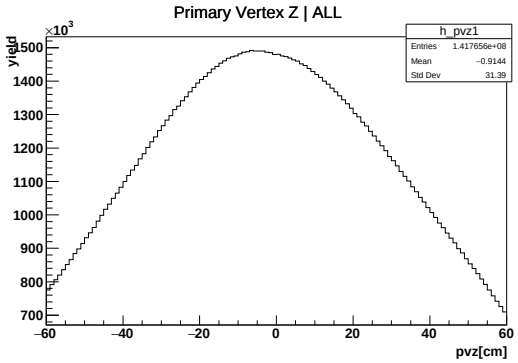

Figure 2.2: z of primary vertex combined four JP trigger samples

2.2 Beam polarization

Beam polarizations are average values over fills with run events used in the analysis weighted. The beam polarizations are 64.35% for blue beam and 58.38% for yellow beam.

We use measurements on the website: `http://www.phy.bnl.gov/cnipol/fills/?rp=12&fn=&ft=1&be=100&mode=1&sb=Select`

2.3 Relative luminosity

In this analysis, due to the lack of the scaler files for parts of the runs, the Jet-Patch events without Λ or $\bar{\Lambda}$ candidates was used to estimate the relative luminosities. The relative luminosities of R_4, R_5 and R_6 are defined as

$$R_4 = \frac{\mathscr{L}^{\uparrow\uparrow}}{\mathscr{L}^{\downarrow\downarrow}} = \frac{n^{\uparrow\uparrow}}{n^{\downarrow\downarrow}} \tag{2.1}$$

$$R_5 = \frac{\mathscr{L}^{\downarrow\uparrow}}{\mathscr{L}^{\downarrow\downarrow}} = \frac{n^{\downarrow\uparrow}}{n^{\downarrow\downarrow}} \tag{2.2}$$

$$R_6 = \frac{\mathscr{L}^{\uparrow\downarrow}}{\mathscr{L}^{\downarrow\downarrow}} = \frac{n^{\uparrow\downarrow}}{n^{\downarrow\downarrow}} \tag{2.3}$$

At first, the pp events without Λ or $\bar{\Lambda}$ candidates were counted for the four spin states of crossing bunches. Then the relative luminosities obtained by using the Eq. 2.1-2.3. The three relative luminosities are shown in Fig. 2.3. The counts of the four spin states and three relative luminosities can be found in Appendix.

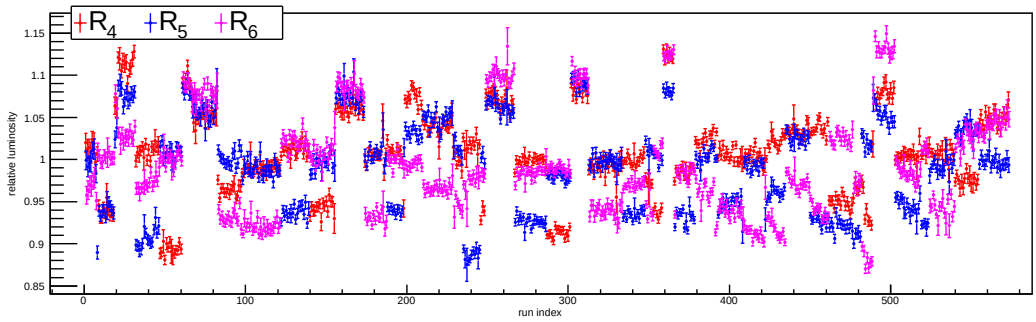

Figure 2.3: Relative luminosities calculated using the Jet-Patch events without Λ or $\bar{\Lambda}$ candidates. They are used to form the single spin collision events.

3 $\Lambda\,(\bar{\Lambda})$ Reconstruction and Jet Correlation

3.1 $\Lambda\,(\bar{\Lambda})$ Reconstruction

The reconstruction was done similarly with the previous longitudinal spin transfer analysis [5]. The candidates were identified from the topology of their dominant weak decay channels, $\Lambda \to p\pi^-$ and $\bar{\Lambda} \to \bar{p}\pi^+$ each having a branching ratio of 63.9%. A search was made in each event to find (anti-)proton and pion tracks of opposite curvatures with an identification cut on track's $d\mathrm{E}/dx$ measured in TPC. The tracks were paired to form $\Lambda\,(\bar{\Lambda})$ candidates and then topological selections were applied to further reduce the background. The topological selections include criteria for the distance of closest approach between the paired tracks and the distance between the middle point of the closest approach and the beam collison vertex, and demanded that the momentum sum of the track pair pointed at the collision vertex. The criteria were tuned in each p_{T} bin to preserve signals in the mass window while reducing the background fraction to 10% or less. The cuts were summarized in TABLE. 3.1 for all the JP samples and the sketch picture Fig. 3.1.

Table 3.1: Summary of selection cuts for $\Lambda\,(\bar{\Lambda})$ reconstruction for Jet-Patch trigger data sample. Here "DCA" denotes "distance of closest approach", "PV" denotes "primary vertex", $\vec{r}$ denotes the vector from primary vertex to the V0 vertex and $\vec{p}$ denotes the momentum vector of V0. Fig. 3.1 shows definitions of topological selection cuts as a reference.

Cut \ p_{T} [GeV/c]	$(1,2)$	$(2,3)$	$(3,4)$	$(4,5)$	$(5,6)$	$(6,8)$
N(hits) of daughter tracks	>14	>14	>14	>14	>14	>14
N(σ) dE/dx for daughters	<3	<3	<3	<3	<3	<3
DCA of V0-daughters [cm]	<0.80	<0.70	<0.60	<0.50	<0.45	<0.45
DCA of V0 to PV [cm]	<1.0	<1.0	<1.0	<1.0	<1.0	<1.0
$\cos(\vec{r},\vec{p})$	>0.995	>0.995	>0.995	>0.995	>0.995	>0.995
Decay Length [cm]	>3.5	>4.0	>4.0	>4.5	>5.0	>5.0
DCA of $p\,(\bar{p})$ to PV [cm]	>0.25	>0.20	>0.10	>0.05	>0.05	>0.05
DCA of π^- (π^+) to PV [cm]	>0.60	>0.55	>0.50	>0.50	>0.50	>0.50
Momentum of π^- (π^+) [GeV/c]	>0.15	>0.15	>0.20	>0.25	>0.30	>0.40

The invariant mass distributions of Λ and $\bar{\Lambda}$ candidates for the trigger-combined sample are shown in Fig. 3.2. The distributions of the invariant mass in each JP trigger samples could be found from the link:
`http://www.star.bnl.gov/protected/spin/jcmei/pp200trans_2012/htmlCode/pp200trans_2012_rec_step_all_cut_crp0995_J0.html`

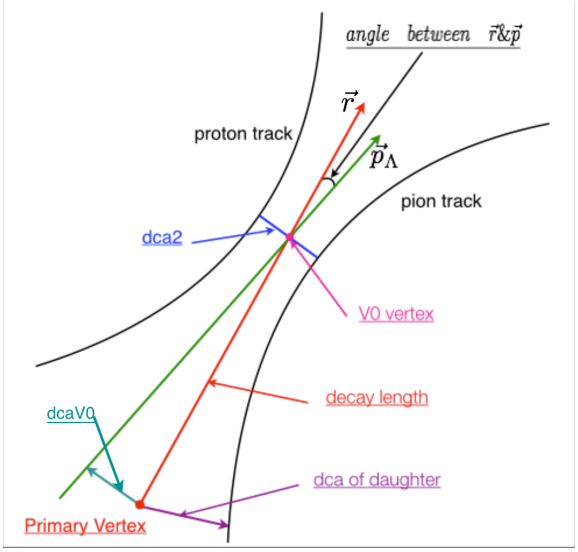

Figure 3.1: Sketch of topological cuts applied in the reconstruction of Λ and $\bar{\Lambda}$.

Table 3.2: Λ and $\bar{\Lambda}$ candidate counts, residual background fractions and signal mass windows after topological selection.

p_{T} [GeV/c]	Λ		$\bar{\Lambda}$		mass window [GeV/c^2]
	counts	bkg. frac.	counts	bkg. frac.	
$(1, 2)$	2378150	0.057	1827999	0.082	$(1.111, 1.119)$
$(2, 3)$	833695	0.066	783074	0.075	$(1.111, 1.121)$
$(3, 4)$	308065	0.066	290993	0.071	$(1.109, 1.123)$
$(4, 5)$	108569	0.065	94996	0.066	$(1.108, 1.124)$
$(5, 6)$	42417	0.073	32733	0.077	$(1.106, 1.126)$
$(6, 8)$	26136	0.090	17187	0.107	$(1.104, 1.128)$

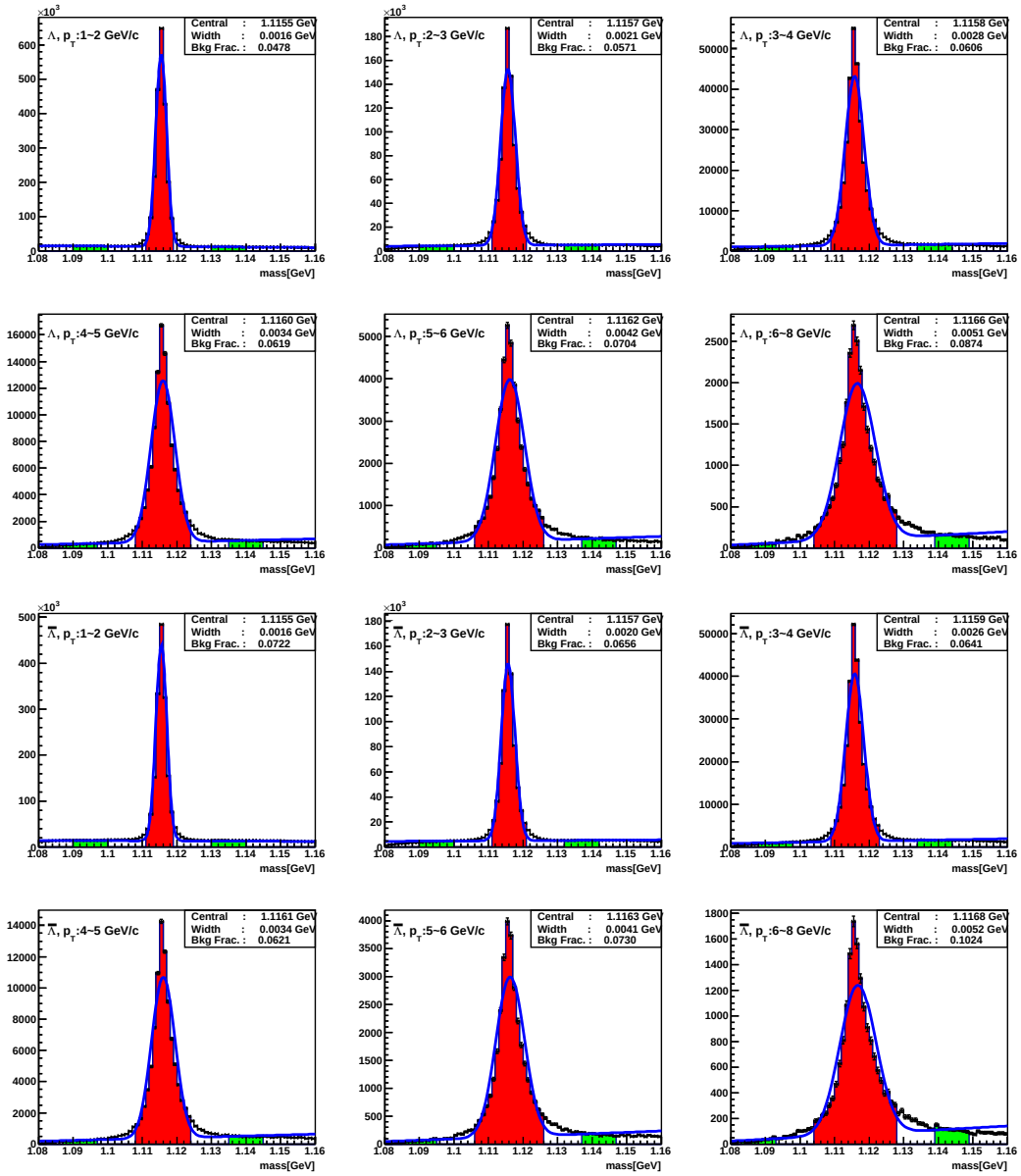

Figure 3.2: Invariant mass distributions of Λ and $\bar{\Lambda}$ candidates after topological selections for the trigger-combined sample.

3.2 Jet Correlation

In our analysis, the outgoing quark momentum dirction is used to determine the polarization direction of $\Lambda\,(\bar{\Lambda})$. In STAR experiment, the tracks in TPC and the energy deposits in EMC towers are used to reconstruct jets using the anti-k_{T} algorithm with a resolution parameter $R = 0.6$. The jets used in this analysis is the public jet tree of pp200GeV_2012 which was generated by J. Kevin Adkins. Fig. 3.3, 3.4 and 3.5 show the p_{T}, η and ϕ distribution of reconstructed jets.

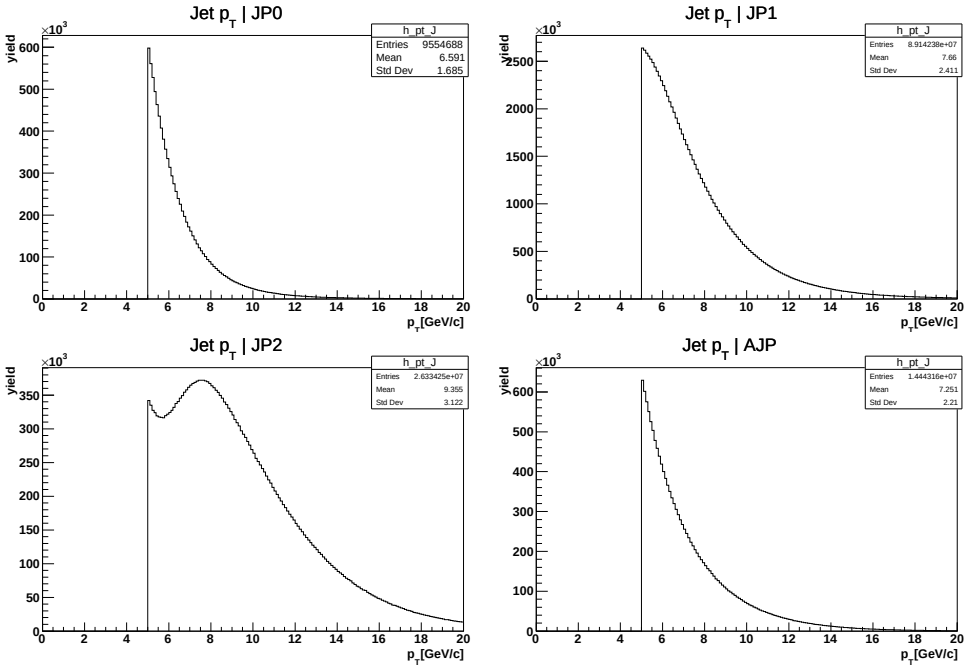

Figure 3.3: p_{T} distribution of reconstructed jets.

The selection cuts applied on jets include $-0.7 < \eta < 0.9$, $E_{\mathrm{T}} > 5\,\mathrm{GeV}$, $0.1 < EMF < 0.95$. EMF is the neutral energy fraction of jet, and it is defined as the ratio of BEMC and EEMC E_{T} sum over the jet E_{T}.

The correlation between $\Lambda\,(\bar{\Lambda})$ candidates and the reconstructed jets is made by constraining the distance $\Delta R(=\sqrt{(\Delta\eta)^2+(\Delta\phi)^2})$ between momentum directions of $\Lambda\,(\bar{\Lambda})$ candidates and jets in $\eta-\phi$ space. The ΔR distributions of $\Lambda\,(\bar{\Lambda})$ from JP1 sample are shown in Fig. 3.6 as an example.

The $\Lambda\,(\bar{\Lambda})$ hyperons in the jet near-side $(\Delta R < 0.6)$ are used to measure D_{TT}. The fraction of jet near-side $\Lambda\,(\bar{\Lambda})$ is increasing with p_{T} increasing. This is beacause $\Lambda\,(\bar{\Lambda})$ with higher p_{T} is more likely from a jet. We note that jet reconstruction in STAR uses the sample of primary tracks in an event, which often includes the $p\,(\bar{p})$ from $\Lambda\,(\bar{\Lambda})$ decay but not the decay pion. In additional, the annihilation effect of $\bar{p}$ in EMC, which provides additional energy to the JP trigger compared to $\Lambda\,(p)$ case leads to an excess of $\bar{\Lambda}$ counts to Λ's in lower p_{T} range. With the increase of p_{T}, the fraction of the energy

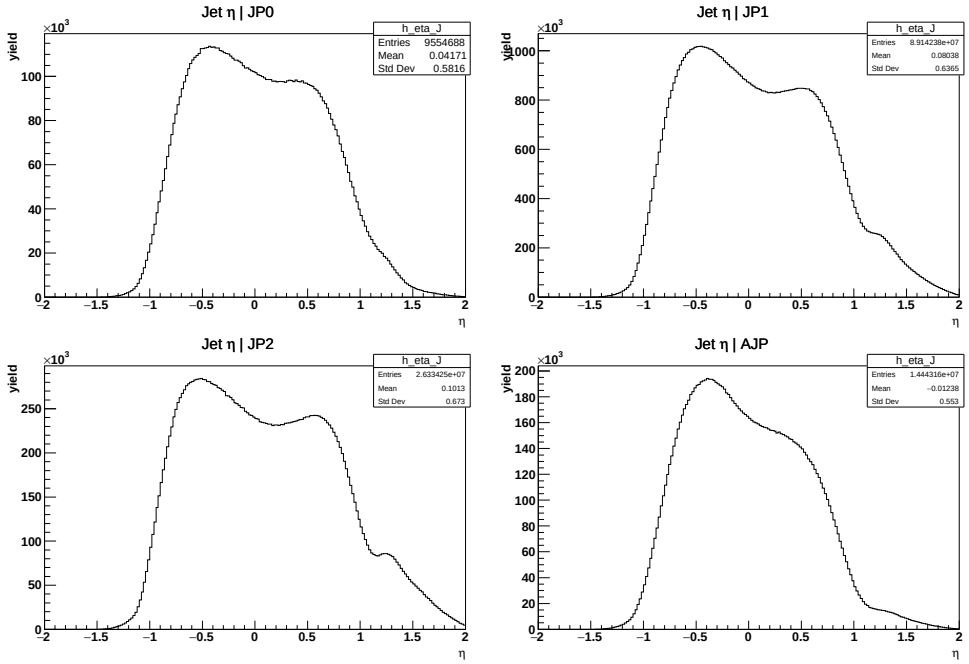

Figure 3.4: η distribution of reconstructed jets.

contributed from the annihilation effect of $\bar{p}$ in the whole energy deposits in EMC is becoming smaller, so the counts of Λ becomes larger than $\bar{\Lambda}$ in higher p_{T} range. No attempt was made to correct the jet or revise the jet finding and reconstruction for these effects. After such requirements, the invariant mass distributions of Λ and $\bar{\Lambda}$ from all JP samples are shown in Fig. 3.7 and the sum number of $\Lambda\,(\bar{\Lambda})$ candidates from all JP data with the residual background fractions in mass windows for each p_{T} bin is listed in Table 3.3. The fractions of Λ and $\bar{\Lambda}$ hyperons falling in jet near-side cone is shown in TABLE 3.4.

The distributons of p_{T}, η and ϕ for the jet near-side Λ and $\bar{\Lambda}$ candidates are shown in Fig. 3.8, 3.9 and 3.10.

The distributions in each JP trigger samples could be found from the link:
`http://www.star.bnl.gov/protected/spin/jcmei/pp200trans_2012/htmlCode/pp200trans_2012_rec_step_all_cut_crp0995_J1.html`

3.3 Control sample: K^0_S

A null-measurement was performed of the spin transfer for the spinless K^0_S meson, which has a similar event topology with Λ hyperon. The decay channel

$$K^0_S \to \pi^+\pi^-$$

Table 3.3: Jet near-side Λ and $\bar{\Lambda}$ candidate counts, residual background fractions and signal mass windows.

p_{T} [GeV/c]	Λ		$\bar{\Lambda}$		mass window [GeV/c^2]
	counts	bkg. frac.	counts	bkg. frac.	
(1, 2)	469681	0.065	502226	0.074	(1.111, 1.119)
(2, 3)	318358	0.079	368042	0.077	(1.111, 1.121)
(3, 4)	181550	0.071	193221	0.072	(1.109, 1.123)
(4, 5)	77866	0.065	71833	0.066	(1.108, 1.124)
(5, 6)	32441	0.070	25571	0.075	(1.106, 1.126)
(6, 8)	20256	0.084	13486	0.102	(1.104, 1.128)

Table 3.4: The fraction of hyperons falling in the jet near-side cone for Λ and $\bar{\Lambda}$ in each p_{T} bin.

p_{T} [GeV/c]	[1,2)	[2,3)	[3,4)	[4,5)	[5,6)	[6,8)
Λ	19.75%	38.19%	58.93%	71.72%	76.48%	77.50%
$\bar{\Lambda}$	27.47%	47.00%	66.40%	75.62%	78.12%	78.47%

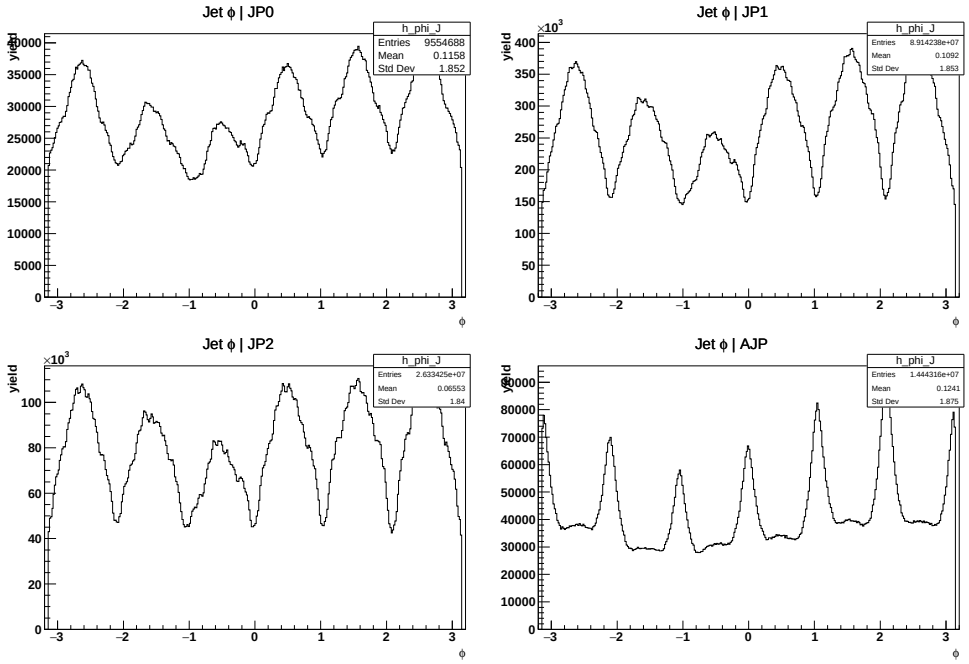

Figure 3.5: ϕ distribution of reconstructed Jets.

with the branching ratio of 69.20 %. The topological selection cuts applied on the reconstruction of the K_S^0 are shown in Table 3.5.

The invavriant mass distribution of K_S^0 is shown in Fig. 3.11.

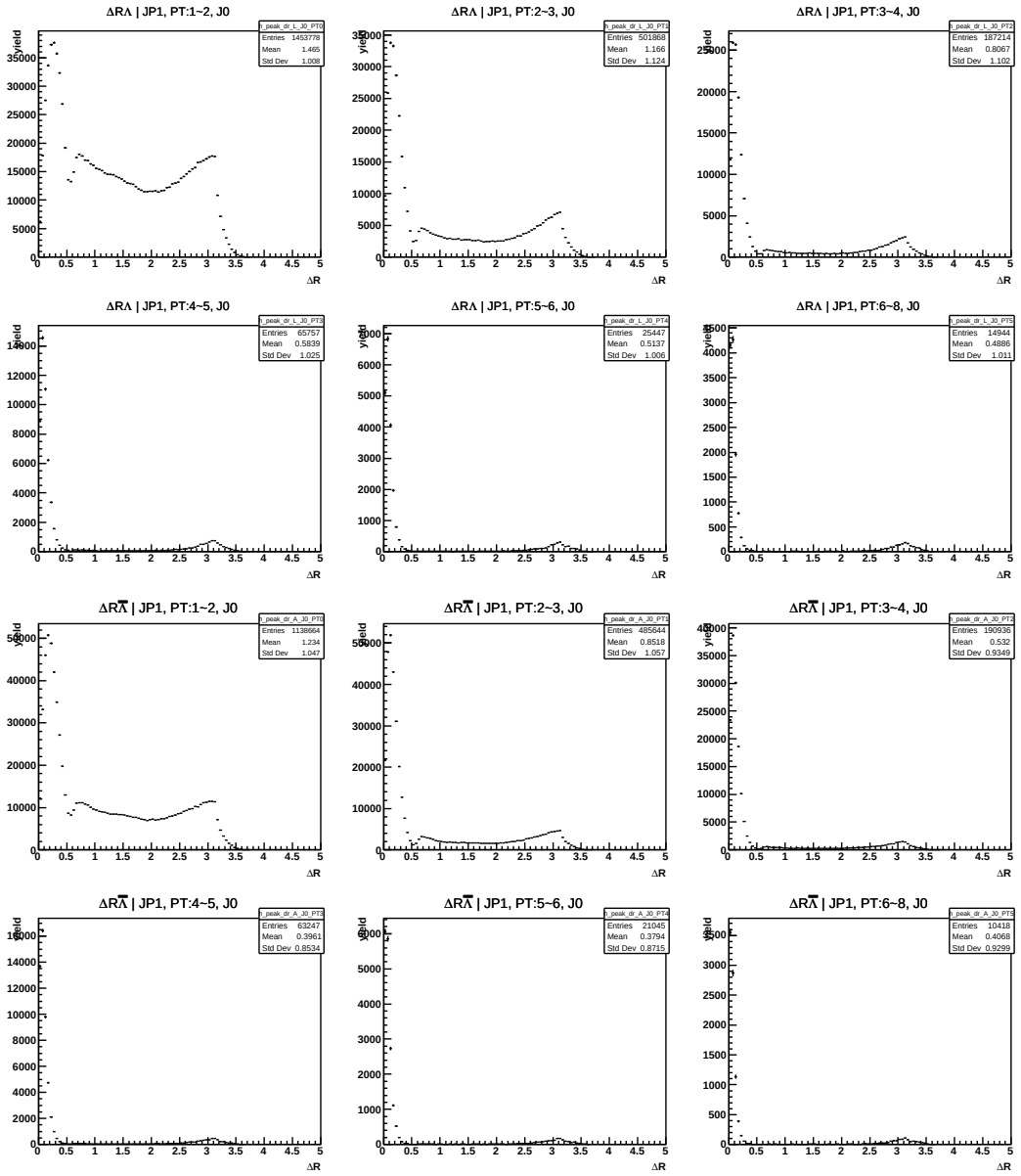

Figure 3.6: ΔR distribution in the correlation between the reconstructed jet and $\Lambda\,(\bar{\Lambda})$ from JP1 trigger sample as the example.

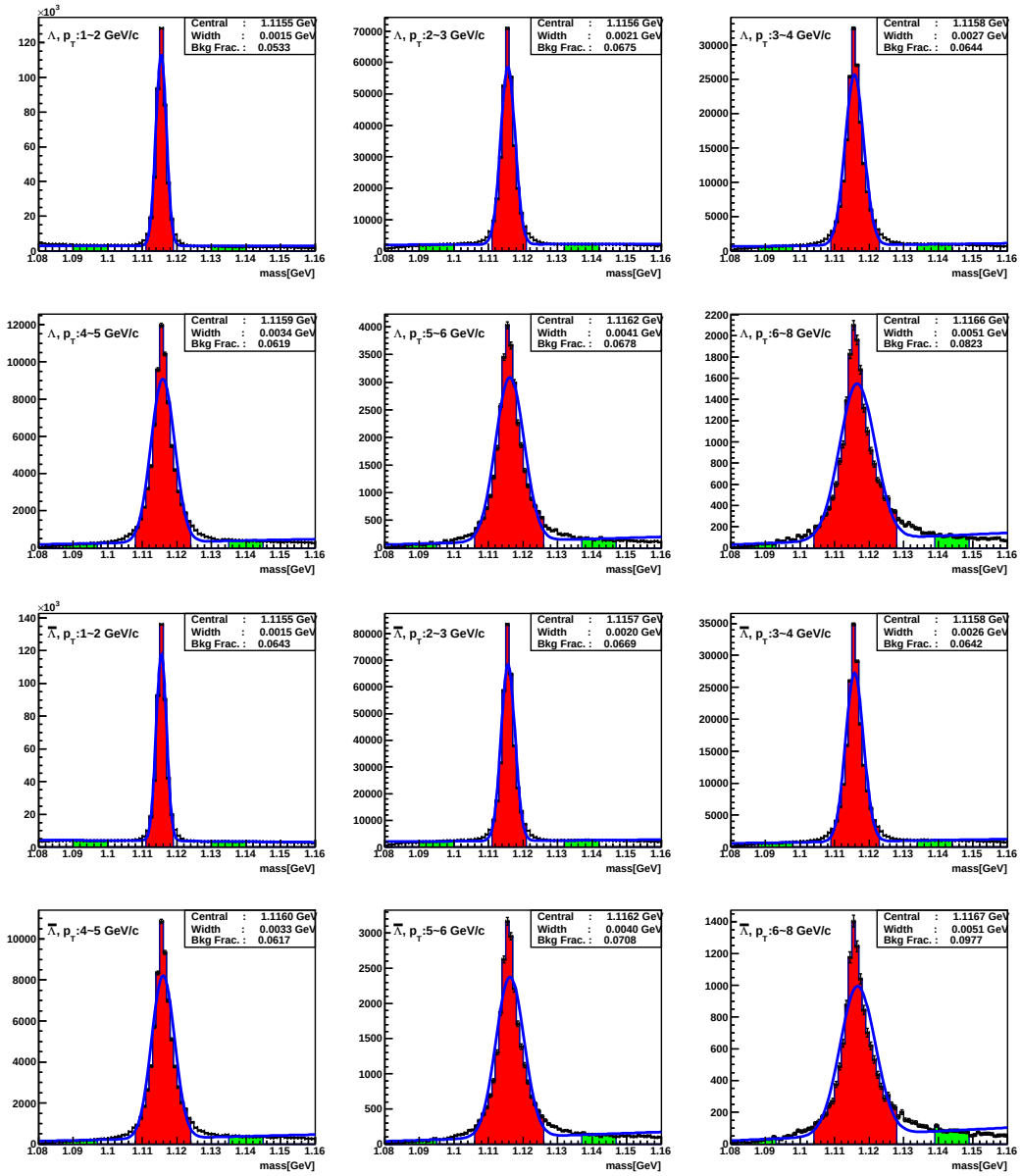

Figure 3.7: The invariant mass distributions of jet near-side Λ and $\bar{\Lambda}$ candidates for the trigger-combined samples.

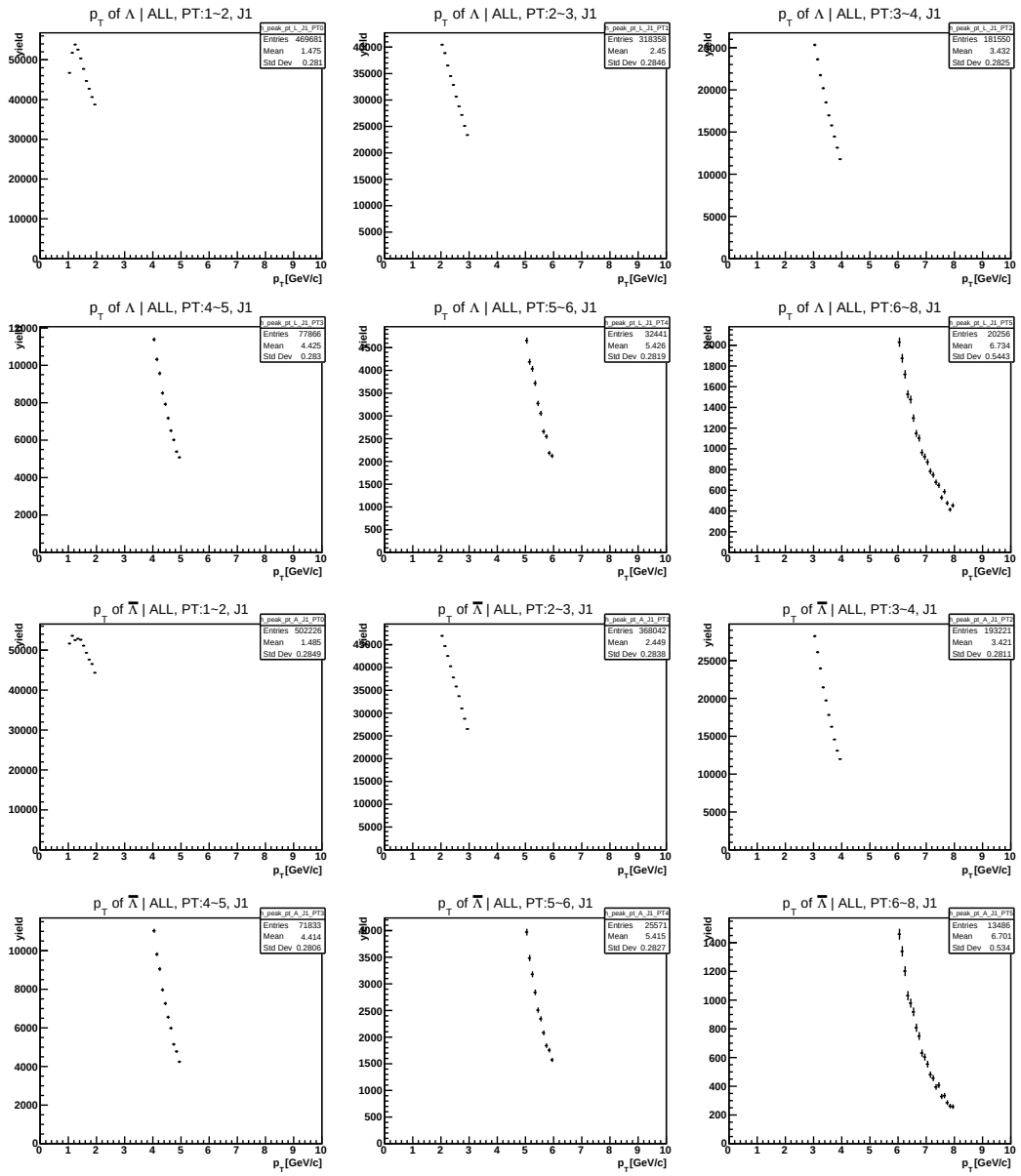

Figure 3.8: The p_{T} distributions of Λ and $\bar{\Lambda}$ candidates in the jet near-side from the four JP trigger samples.

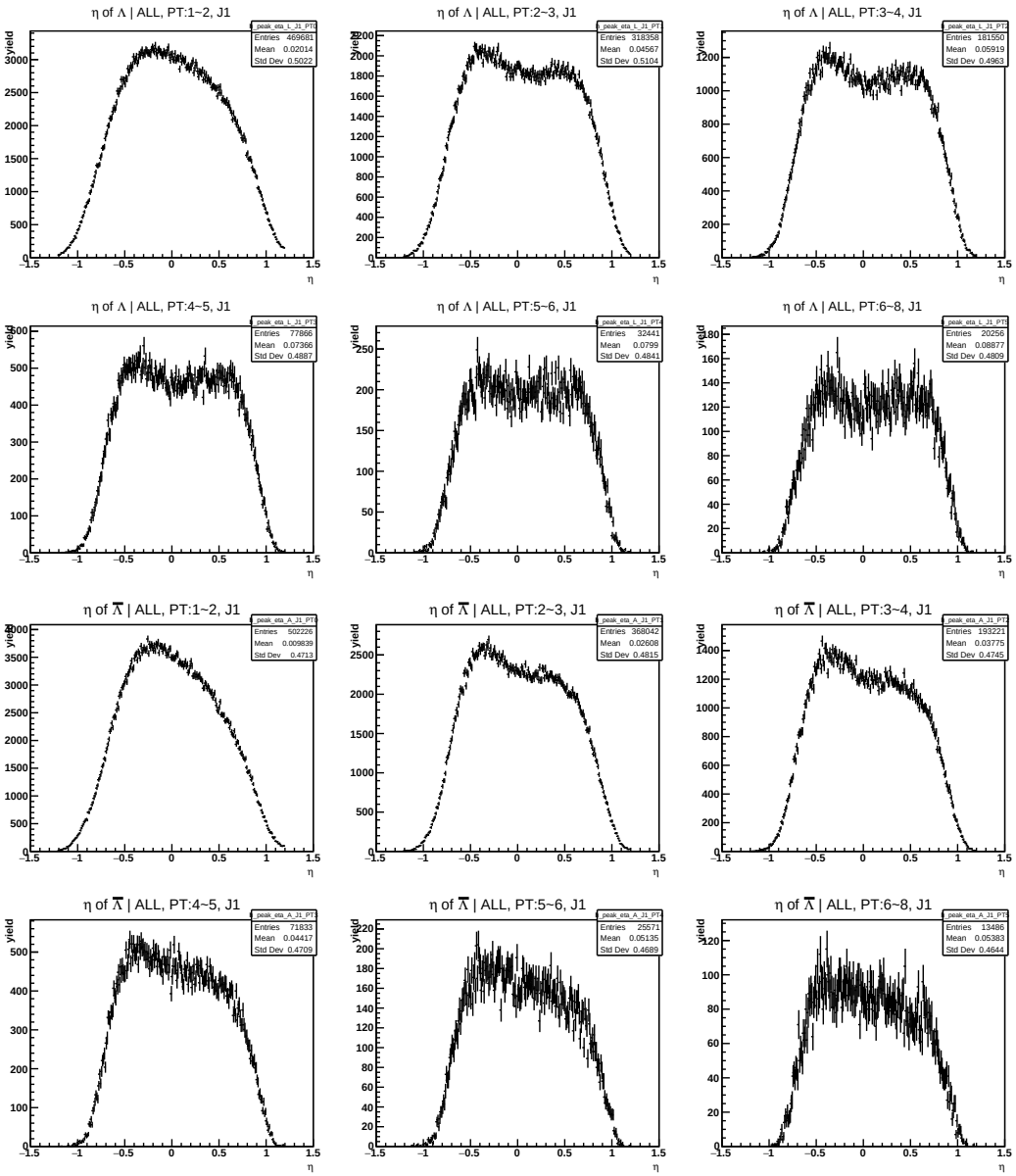

Figure 3.9: The η distributions of Λ and $\bar{\Lambda}$ candidates in the jet near-side from the four JP trigger samples.

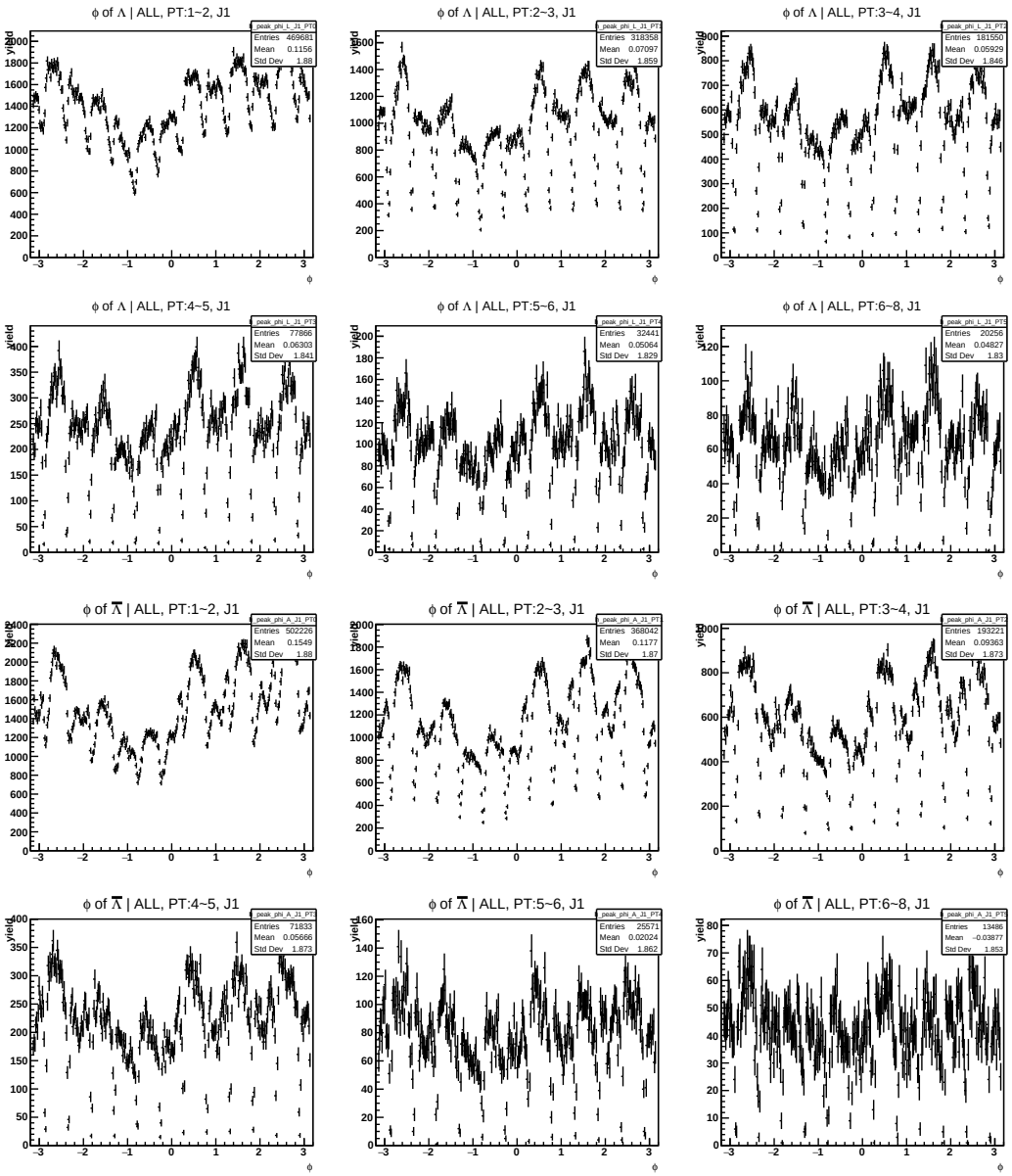

Figure 3.10: The ϕ distributions of Λ and $\bar{\Lambda}$ candidates in the jet near-side from the four JP trigger samples.

Table 3.5: Summary of selection cuts for K^0_S reconstruction for Jet-Patch trigger data sample. Here "DCA" denotes "distance of closest approach", "PV" denotes "primary vertex", $\vec{r}$ denotes the vector from primary vertex to the V0 vertex and $\vec{p}$ denotes the momentum vector of V0. Fig. 3.1 shows definitions of topological selection cuts as a reference.

Cut \ p_{T} [GeV/c]	(1, 2)	(2, 3)	(3, 4)	(4, 5)	(5, 6)	(6, 8)
N(hits) of daughter tracks	>14	>14	>14	>14	>14	>14
N(σ) dE/dx for daughters	<3	<3	<3	<3	<3	<3
DCA of V0-daughters [cm]	<0.70	<0.65	<0.55	<0.45	<0.40	<0.35
DCA of V0 to PV [cm]	<0.60	<0.70	<0.80	<0.80	<0.80	<0.80
cos $(\vec{r}, \vec{p})$	>0.99	>0.99	>0.99	>0.99	>0.99	>0.99
Decay Length [cm]	>1.20	>1.40	>1.50	>1.60	>1.80	>2.00
DCA of π^- (π^+) to PV [cm]	>0.60	>0.55	>0.50	>0.45	>0.40	>0.35
Momentum of π^- (π^+) [GeV/c]	>0.15	>0.15	>0.20	>0.25	>0.30	>0.40

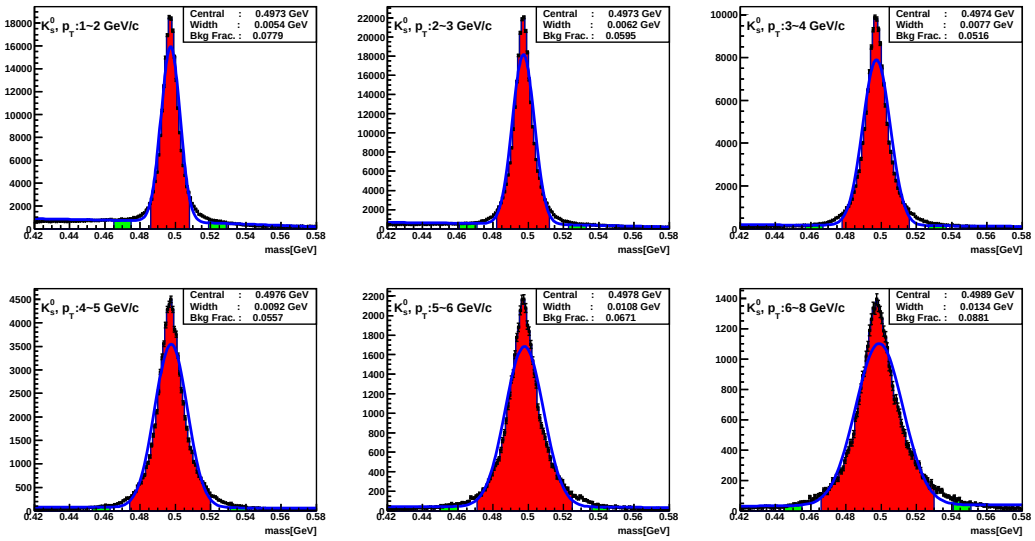

Figure 3.11: Invariant mass of K^0_S candidates for the trigger-combined sample.

4 Extraction of Transverse Spin Transfer

Usually, the polarization and spin transfer of $\Lambda\,(\bar{\Lambda})$ can be measured via its weak decay channel $\Lambda \to p\pi^-$ ($\bar{\Lambda} \to \bar{p}\pi^+$) from the angular distribution of the final state,

$$\frac{dN}{d\cos\theta^*} = \frac{N_{\rm tot}}{2} A(\cos\theta^*)(1 + \alpha_\Lambda P_\Lambda \cos\theta^*), \tag{4.1}$$

where $N_{\rm tot}$ is the total number of Λ produced in collisions, $\alpha_\Lambda = -\alpha_{\bar{\Lambda}} = 0.642 \pm 0.013$ [4] is the decay parameter, θ^* is the angle between the decay proton momentum in the Λ's rest frame and the Λ polarization direction (Fig. 3.1) and $A(\cos\theta^*)$ is the detector acceptance which may vary with θ^* as well as other observables. The average of the detector acceptence shows as:

$$\langle A(P, \cos\theta^*)\rangle = \frac{\int A(\cos\theta^*) N(P, \cos\theta^*) d\cos\theta^*}{\int N(P, \cos\theta^*) d\cos\theta^*}, \tag{4.2}$$

where $N(P, \cos\theta^*)$ is the number of Λ with beam polarization P and $\cos\theta^*$. The acceptance is expected to be a constant in a small $\cos\theta^*$ interval $[\theta_1^*, \theta_2^*)$ and the average of the acceptance is used, which is noted as $\langle A(P, \cos\theta_1^*, \cos\theta_2^*)\rangle$. Then the number of Λ with the inversed polarization in the small interval $[\cos(\theta_1^*), \cos(\theta_2^*)]$ could be obtained

$$\begin{aligned} N(P) &= \langle A(P, \cos\theta_1^*, \cos\theta_2^*)\rangle N_{tot}(\cos\theta_2^* - \cos\theta_1^*) + \frac{\alpha}{2} P(\cos^2\theta_2^* - \cos^2\theta_1^*) \\ N(-P) &= \langle A(-P, \cos\theta_1^*, \cos\theta_2^*)\rangle N_{tot}(\cos\theta_2^* - \cos\theta_1^*) - \frac{\alpha}{2} P(\cos^2\theta_2^* - \cos^2\theta_1^*). \end{aligned} \tag{4.3}$$

Due to the symmetry of the detector geometry, the acceptances of the inversed polarizations should be the same, namely $\langle A(P, \cos\theta_1^*, \cos\theta_2^*)\rangle = \langle A(-P, \cos\theta_1^*, \cos\theta_2^*)\rangle$. Thus the asymmetry of inversed polarizations is

$$\frac{N(P) - N(-P)}{N(P) + N(-P)} = \alpha P_\Lambda \frac{\cos\theta_1^* + \cos\theta_2^*}{2}, \tag{4.4}$$

Further, the polarization of Λ can be expressed as:

$$P_\Lambda = \frac{1}{\alpha\langle\cos\theta^*\rangle} \frac{N(P) - N(-P)}{N(P) + N(-P)}, \tag{4.5}$$

where $\langle\cos\theta^*\rangle$ is the average value of $\cos\theta^*$ in a small interval $[\theta_1^*, \theta_2^*]$. In Eq. 4.5, the acceptance of the detector has been cancelled. In the pp collision, the polarization of Λ will be inversed with the polarization of incoming proton inversed, namely

$$P_\Lambda(p^\uparrow p \to \Lambda X) = -P_\Lambda(p^\downarrow p \to \Lambda X) \tag{4.6}$$

The Λ polarization in experiment is transferred from the beam polarization

$$P_\Lambda = D_{\rm TT} P, \tag{4.7}$$

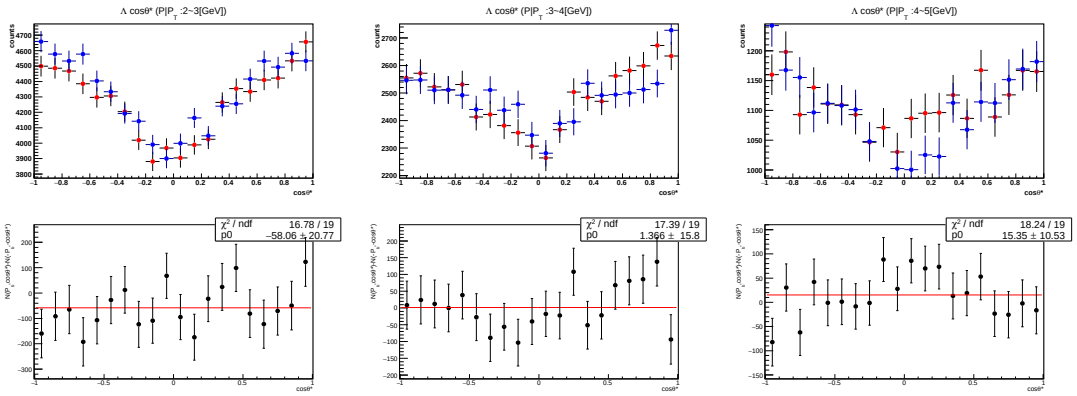

Figure 4.1: Symmetry test of Λ counts when both of the beam polarization and $\cos\theta^*$ reverse.

where D_{TT} is actually the ratio of beam polarization transferred to Λ polarization.

To minimize the uncertainty associated with the detector acceptance effects, D_{TT} has been extracted through the asymmetry of Λ counts in small $\cos\theta^*$ intervals with opposite beam polarization:

$$D_{\mathrm{TT}} = \frac{1}{\alpha P \langle \cos\theta^* \rangle} \frac{N^{\uparrow} - RN^{\downarrow}}{N^{\uparrow} + RN^{\downarrow}}, \tag{4.8}$$

where α is the decay parameter [4], P is the polarization of the beam, $\langle \cos\theta^* \rangle$ is the average value in each small $\cos\theta^*$ bin, $N^{\uparrow}(N^{\downarrow})$ are the counts of hyperons in a small $\cos\theta^*$ interval when the beam is positively (negatively) polarized and R is the relative luminosity ratio for these two polarization states. The detector acceptance in this $\cos\theta^*$ interval is largely canceled because the acceptance in a small $\cos\theta^*$ interval is expected to be the same when flipping the beam spin.

In this analysis, the cross-ratio method is used to extract D_{TT} and thus the relative luminosity R Eq. 4.8 can be canceled. Based on the symmetry of the cross section of hyperon when both of beam polarization and $\cos\theta^*$ reverse, namely

$$\sigma^{\uparrow}(\cos\theta^*) = \sigma^{\downarrow}(-\cos\theta^*), \quad \sigma^{\downarrow}(\cos\theta^*) = \sigma^{\uparrow}(-\cos\theta^*), \tag{4.9}$$

where σ is the cross section of hyperons and $\uparrow$ ($\downarrow$) is the beam polarization direction. The symmetry can be tested using the hyperon counts distribution with $\cos\theta^*$. The symmetries are shown in Fig. 4.1 and Fig. 4.2 for Λ and $\bar{\Lambda}$ correspondingly. The symmetries are good within the uncertainty. Then from the following equation Eq. 4.10 and Eq. 4.13, we could find that the relative luminosities are canceled when single beam is polarized.

$$\sigma^{\uparrow} = \frac{N^{\uparrow}}{\mathscr{L}^{\uparrow}}, \quad \sigma^{\downarrow} = \frac{N^{\downarrow}}{\mathscr{L}^{\downarrow}}, \tag{4.10}$$

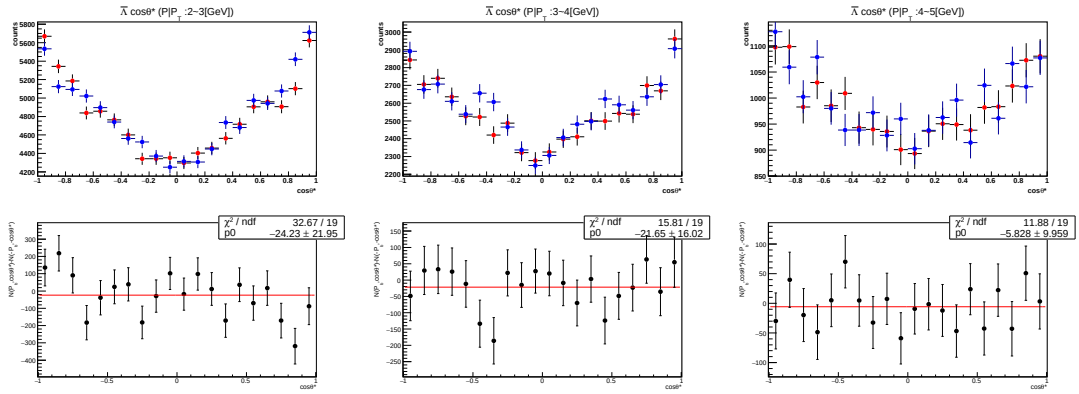

Figure 4.2: Symmetry test of $\bar{\Lambda}$ counts when both of the beam polarization and $\cos\theta^*$ reverse.

$$\frac{\sqrt{\sigma^{\uparrow}(\cos\theta^*)\sigma^{\downarrow}(-\cos\theta^*)} - \sqrt{\sigma^{\uparrow}(-\cos\theta^*)\sigma^{\downarrow}(\cos\theta^*)}}{\sqrt{\sigma^{\uparrow}(\cos\theta^*)\sigma^{\downarrow}(-\cos\theta^*)} + \sqrt{\sigma^{\uparrow}(-\cos\theta^*)\sigma^{\downarrow}(\cos\theta^*)}} \tag{4.11}$$

$$= \frac{\sqrt{\frac{N^{\uparrow}(\cos\theta^*)}{\mathscr{L}^{\uparrow}}\frac{N^{\downarrow}(-\cos\theta^*)}{\mathscr{L}^{\downarrow}}} - \sqrt{\frac{N^{\uparrow}(-\cos\theta^*)}{\mathscr{L}^{\uparrow}}\frac{N^{\downarrow}(\cos\theta^*)}{\mathscr{L}^{\downarrow}}}}{\sqrt{\frac{N^{\uparrow}(\cos\theta^*)}{\mathscr{L}^{\uparrow}}\frac{N^{\downarrow}(-\cos\theta^*)}{\mathscr{L}^{\downarrow}}} + \sqrt{\frac{N^{\uparrow}(-\cos\theta^*)}{\mathscr{L}^{\uparrow}}\frac{N^{\downarrow}(\cos\theta^*)}{\mathscr{L}^{\downarrow}}}} \tag{4.12}$$

$$= \frac{\sqrt{N^{\uparrow}(\cos\theta^*)N^{\downarrow}(-\cos\theta^*)} - \sqrt{N^{\uparrow}(-\cos\theta^*)N^{\downarrow}(\cos\theta^*)}}{\sqrt{N^{\uparrow}(\cos\theta^*)N^{\downarrow}(-\cos\theta^*)} + \sqrt{N^{\uparrow}(-\cos\theta^*)N^{\downarrow}(\cos\theta^*)}}, \tag{4.13}$$

At last, the equation used to extract D_{TT} is expressed as Eq. 4.14.

$$D_{\mathrm{TT}} = \frac{1}{\alpha P_{\mathrm{beam}}\langle\cos\theta^*\rangle}\frac{\sqrt{N^{\uparrow}(\cos\theta^*)N^{\downarrow}(-\cos\theta^*)} - \sqrt{N^{\uparrow}(-\cos\theta^*)N^{\downarrow}(\cos\theta^*)}}{\sqrt{N^{\uparrow}(\cos\theta^*)N^{\downarrow}(-\cos\theta^*)} + \sqrt{N^{\uparrow}(-\cos\theta^*)N^{\downarrow}(\cos\theta^*)}}, \tag{4.14}$$

Here the approximation

$$\mathscr{L}^{\uparrow\uparrow} \approx \mathscr{L}^{\uparrow\downarrow}, \quad \mathscr{L}^{\downarrow\downarrow} \approx \mathscr{L}^{\downarrow\uparrow}$$

are used here and actually the approximation is highly convinced which is shown in Fig. 4.3. The values of relative luminosities are really closed to each other and the residual polarized parts of the unpolarized beam expected are really small. The residual polarized parts are hardly affect the D_{TT} results especially in the positive η range.

To measure the transverse spin transfer, D_{TT}, the polarization direction of Λ needs to be determined first. Here, the polarization direction of Λ is considered as the same with the polarization direction of the outgoing quark which can be obtained via the rotation relationship with the polarization direction of the incoming quark [3]. At the experimental level, the polarization direction of the beam is substituted for that of the

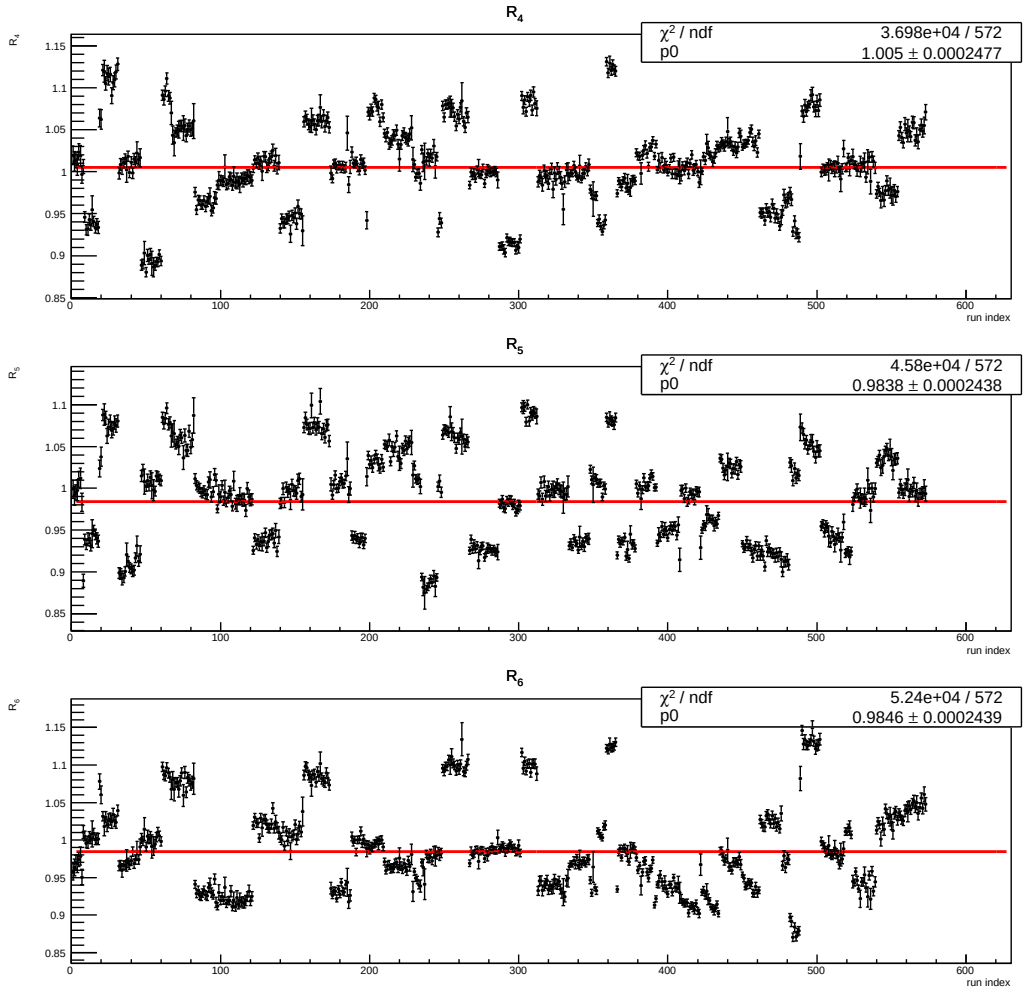

Figure 4.3: Average values of relative luminosities over runs.

incoming quark and the momentum direction of the jet reconstructed is substituted for that of the outgoing quark.

After the reconstruction and jet correlation, the $\Lambda\,(\bar{\Lambda})$ sample was obtained. The $\cos\theta^*$ for each $\Lambda\,(\bar{\Lambda})$ candidate was calulated with the blue and yellow beam as the polarized beam separately. The spin 4-bit sorted distributions were combined using the relative luminosities as the weight to form the distribution sorted by beam polarization. The $\cos\theta^*$ vs. invariant mass distributions and $\cos\theta^*$ distributions of Λ and $\bar{\Lambda}$ for inversed beam polarizations with η of $0 \sim 1.2$, p_{T} of $2 \sim 3\,\mathrm{GeV/c}$ and BLUE beam as the polarized beam from JP1 sample are shown in Fig. 4.4 and Fig. 4.5 are used as examples. The distributions from all Λ p_T and all JP trigger samples bins could be found from the link:
`http://www.star.bnl.gov/protected/spin/jcmei/pp200trans_2012/htmlCode/pp200trans_2012_dttExtraction_1.html`
The distributions of $\cos\theta^*$ versus invariant mass could be found from the link, too. The drop in the middle range ($\cos\theta^* \sim 0$) is due to the missing of the daughter particle with small p_{T}.

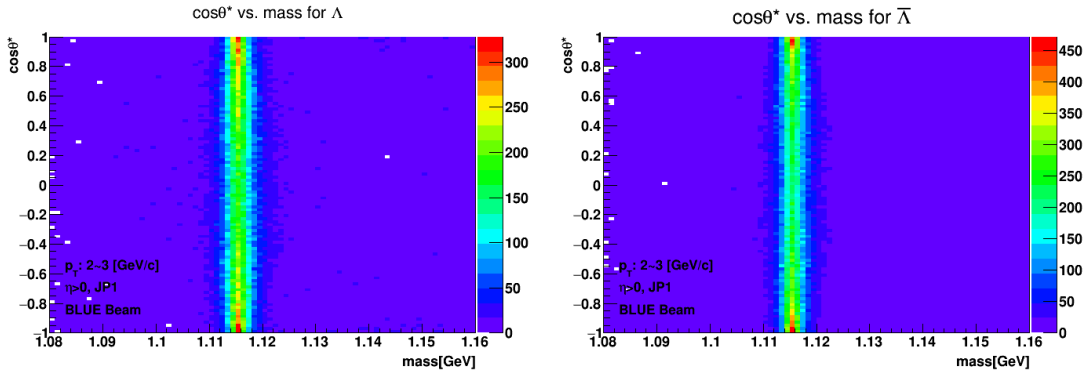

Figure 4.4: $\cos\theta^*$ vs. invariant mass distribution for Λ(left) and $\bar{\Lambda}$(right) with $2 < p_{\mathrm{T}} < 3\,\mathrm{GeV/c}$ and $0 < \eta < 1.2$from JP1 sample with the BLUE beam as the polarized beam.

D_{TT} in each small $\cos\theta^*$ interval were obtained using Eq. 4.8 and shown in Fig. 4.6. Here the results are from JP1 sample and with the Λ p_{T} of $2 \sim 3\,\mathrm{GeV}/c$.

Then D_{TT} in each $\cos\theta^*$ interval are fitted using a constant in each p_{T} bin and the fitted result is used as the D_{TT} for the p_{T} bin. Fig. 4.7 shows the D_{TT} of $\Lambda\,(\bar{\Lambda})$ for JP triggers.

4.1 Trigger Combined D_{TT}

D_{TT} values for each of the JP trigger samples are consistent with each other within the statistical uncertainty and the χ^2 test for the results of each two trigger samples are shown in TABLE 4.1 so we combined the events from each of the trigger samples into one data sample.

The D_{TT} for $\Lambda\,(\bar{\Lambda})$ and δ_{TT} for K^0_S vs. $\cos\theta^*$ in each p_{T} bin are shown in Fig. 4.8.

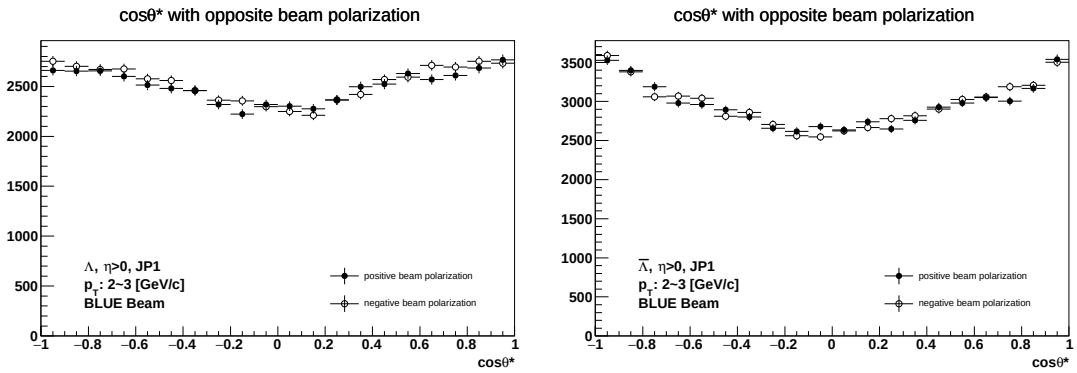

Figure 4.5: $\cos\theta^*$ distribution for (a) Λ and (b) $\bar{\Lambda}$ from JP1 sample. The solid circle denotes the positive beam polarization and the open circle denotes the negative beam polarization.

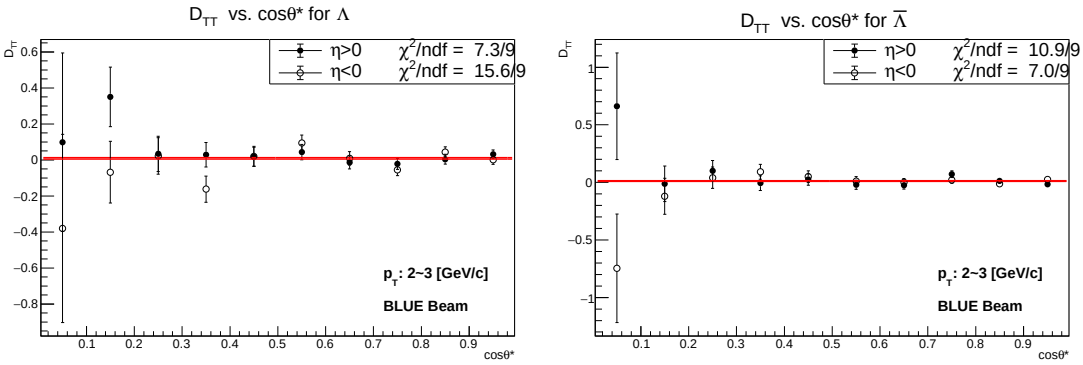

Figure 4.6: D_{TT} vs. $\cos\theta^*$ for Λ(left) and $\bar{\Lambda}$(right) with p_{T} of $2 \sim 3\,\mathrm{GeV/c}$ using JP1 data.

Table 4.1: χ^2/ndf testing between the results of each two trigger samples

Trigger	Λ		$\bar{\Lambda}$	
	$0 < \eta < 1.2$	$-1.2 < \eta < 0$	$0 < \eta < 1.2$	$-1.2 < \eta < 0$
JP0 : JP1	6.47/6	2.58/6	3.84/6	5.94/6
JP0 : JP2	6.09/6	2.48/6	5.85/6	3.09/6
JP0 : AJP	5.02/6	2.97/6	6.10/6	3.47/6
JP1 : JP2	6.68/6	2.60/6	10.45/6	3.27/6
JP1 : AJP	2.70/6	2.86/6	7.84/6	4.62/6
JP2 : AJP	6.57/6	3.80/6	12.56/6	4.23/6

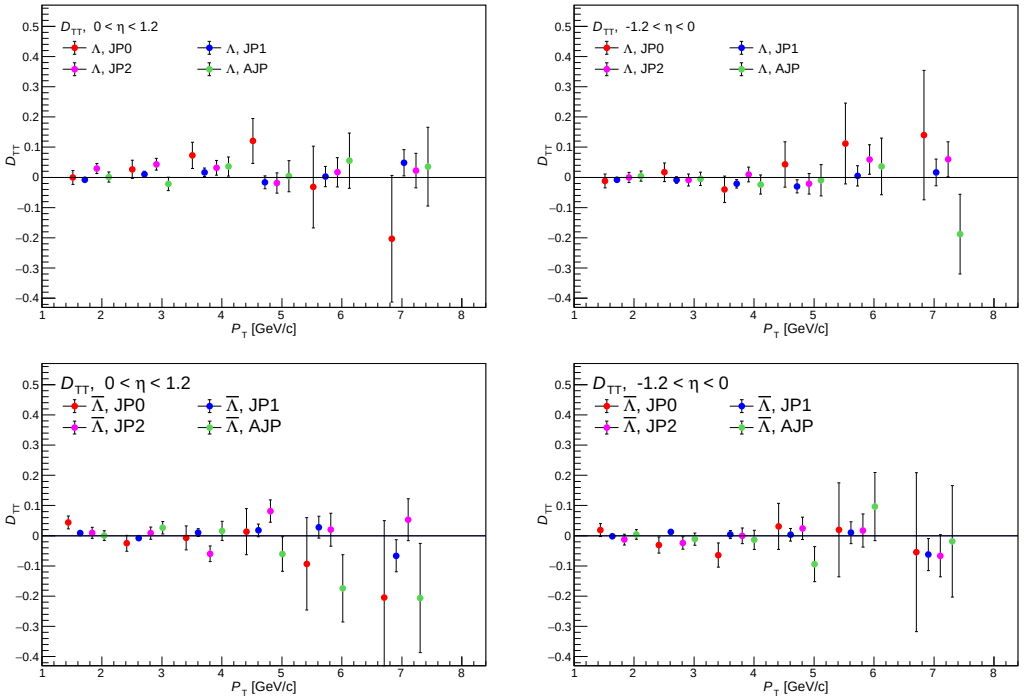

Figure 4.7: D_{TT} for the 4 JP trigger samples. The upper panel is for Λ and the lower is for $\bar{\Lambda}$. The η range is $0 \sim 1.2$ in the left and $-1.2 \sim 0$ in the right.

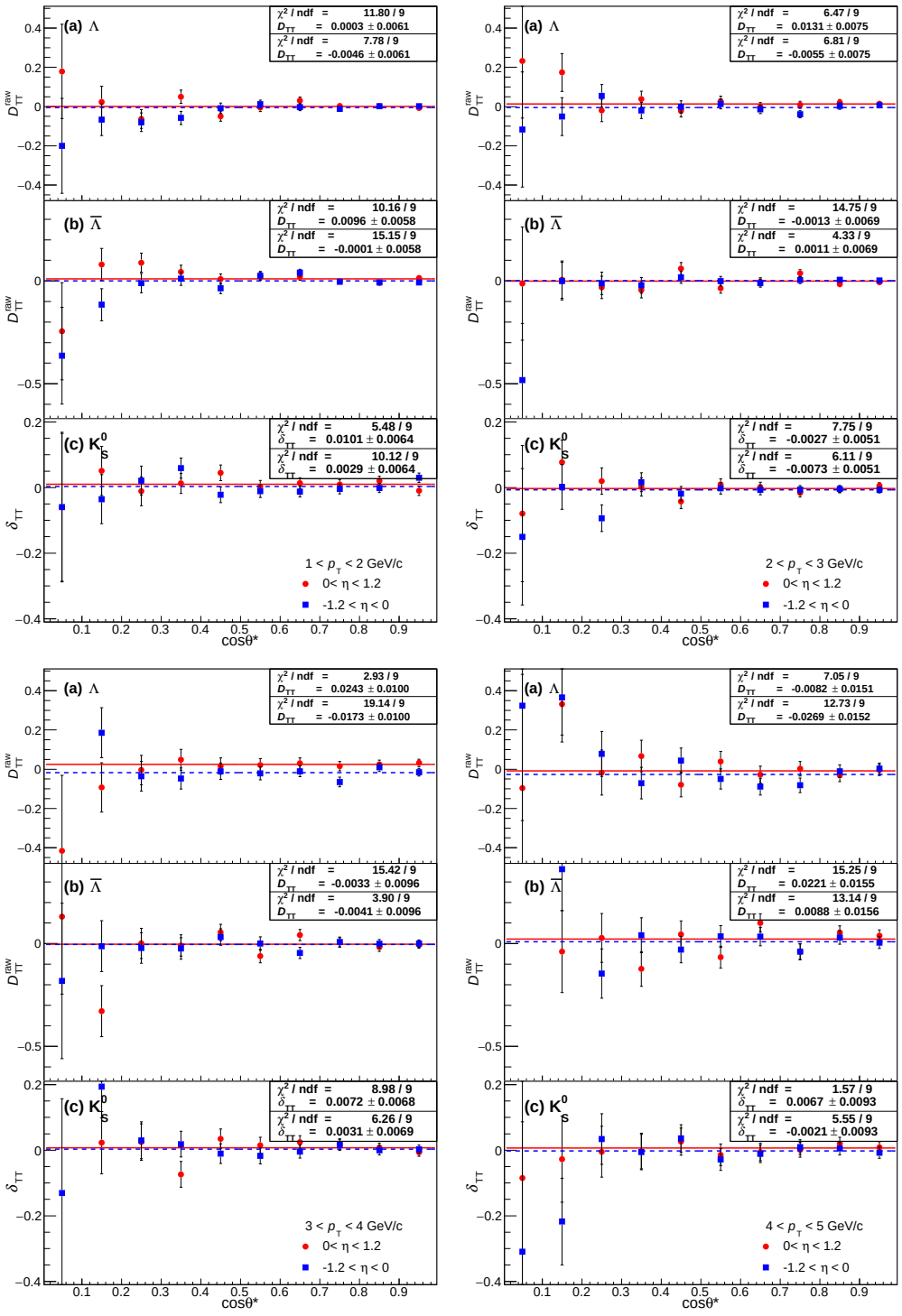

Figure 4.8: D_{TT} for $\Lambda\,(\bar{\Lambda})$ and δ_{TT} for K^0_S vs. $\cos\theta^*$ in each p_{T} bin from the trigger-combined data sample.

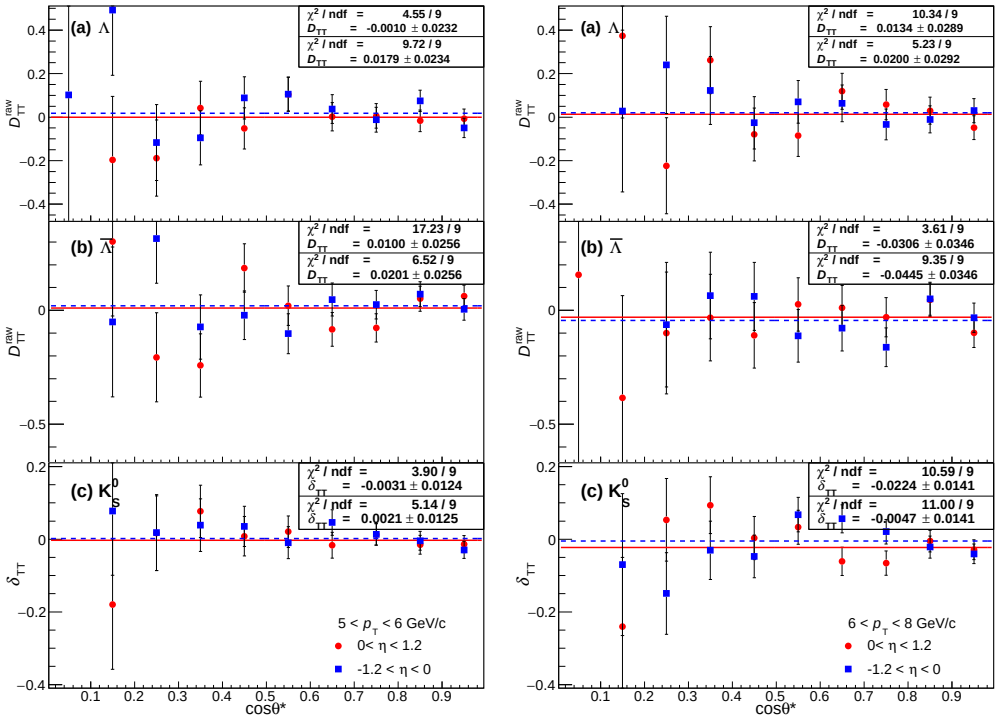

Figure 4.8: D_{TT} for $\Lambda\,(\bar{\Lambda})$ and δ_{TT} for K^0_S vs. $\cos\theta^*$ in each p_{T} bin from the trigger-combined data sample.

D_{TT} extracted from the JP trigger-combined data sample are shown in Fig. 4.9.

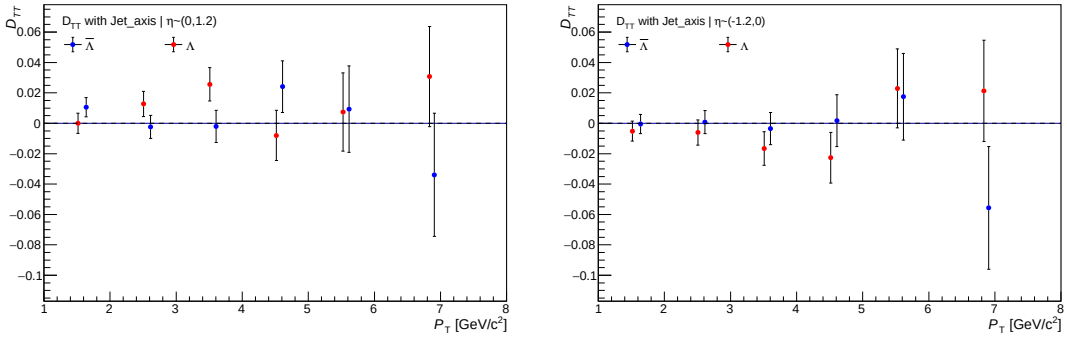

Figure 4.9: D_{TT} for the trigger-combined sample. The left and right plots are for $0 < \eta < 1.2$ and $-1.2 < \eta < 0$, correspondingly.

K^0_S was reconstructed in our analysis which is used to do the cross check. We constructed the so-called "spin asymmetry", δ_{TT}, of K^0_S using the same structure with D_{TT} of Λ shown in Eq. 4.15 where the N is the number of K^0_S reconstructed and $\alpha_{K^0_S}$ is assumed as 1 which used as the decay parameter of Λ.

$$\delta_{\mathrm{TT}} = \frac{1}{\alpha_{K^0_S} P \langle \cos\theta^* \rangle} \frac{\sqrt{N^{\uparrow}(\cos\theta^*)N^{\downarrow}(-\cos\theta^*)} - \sqrt{N^{\uparrow}(-\cos\theta^*)N^{\downarrow}(\cos\theta^*)}}{\sqrt{N^{\uparrow}(\cos\theta^*)N^{\downarrow}(-\cos\theta^*)} + \sqrt{N^{\uparrow}(-\cos\theta^*)N^{\downarrow}(\cos\theta^*)}} \tag{4.15}$$

Higher statistics and lower background fraction make K^0_S a good choice to do the check. The results of δ_{TT} versus p_{T} from trigger combined sample are shown in bottom panels in Fig. 4.8.

4.2 Cross check of D_{TT} measurement method

The main results were extracted via the Cross-Ratio method. We also used the relative luminosity method to extract D_{TT} as the cross check. In the relative luminosity method, D_{TT} in a small $\cos\theta^*$ interval is extracted via the equation following,

$$D_{\mathrm{TT}} = \frac{1}{\alpha P_{\mathrm{beam}} \langle \cos\theta^* \rangle} \frac{(\frac{N^{\uparrow\uparrow}}{R_4} + \frac{N^{\uparrow\downarrow}}{R_6}) - (N^{\downarrow\downarrow} + \frac{N^{\downarrow\uparrow}}{R_5})}{(\frac{N^{\uparrow\uparrow}}{R_4} + \frac{N^{\uparrow\downarrow}}{R_6}) + (N^{\downarrow\downarrow} + \frac{N^{\downarrow\uparrow}}{R_5})}. \tag{4.16}$$

The comparison between the results corresponding to the two methods is shown in Fig. 4.10. The result comparison between the two methods are consistent to each other. This is a good proof to the stabilty of our measurement method.

In the main results extraction, we used the jet axis as the substitute of the quark axis. The results extracted by using the hyperon aixs as the substitute of the quark axis are shown in Fig 4.11 for the cross check and a good agreement is observed in the comparison.

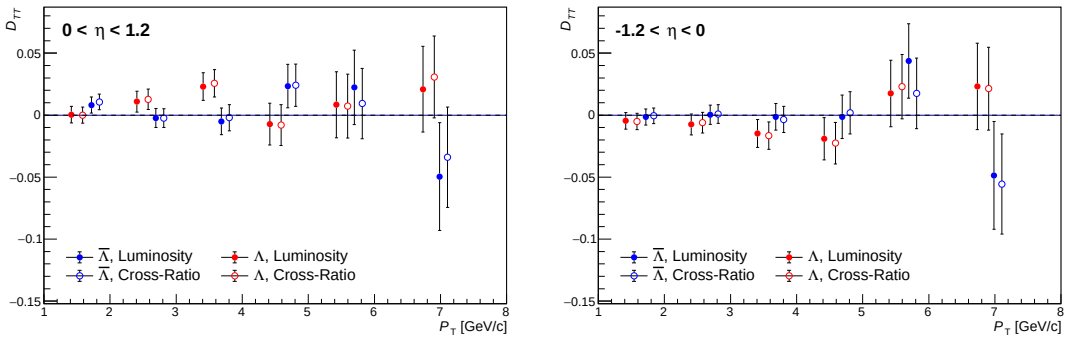

Figure 4.10: The comparison between the results extracted via Cross-Ratio method and Relative Luminosity method. The left and right plots are for $0 < \eta < 1.2$ and $-1.2 < \eta < 0$, correspondingly.

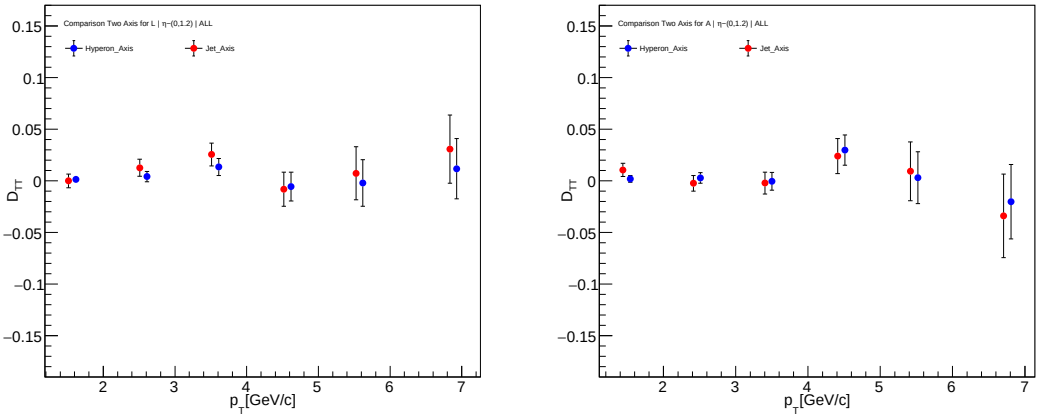

Figure 4.11: The comparison between the results extracted by using the hyperon aixs and the jet axis as the substitute of the quark axis, separately.

5 MC Production and Data Comparison

5.1 MC Production

Private MC sample was generated to compare with data and further do the study of trigger bias. The MC sample was generated using pure pythia of version 6.4.28 [6] with Perugia 2012 tune [7] and GEANT-based simulation framework. The sample was generated in each $\Lambda\, p_{\mathrm{T}}$ and hard p_{T} interval separately and then combined with weight of hard p_{T} in each $\Lambda\, p_{\mathrm{T}}$ interval. The hard p_{T} distributions for each $\Lambda\, p_{\mathrm{T}}$ are shown in Fig. 5.1.

The hard p_{T} does not comply with exponential distribution perfectly. This is because that only $\Lambda\,(\bar{\Lambda})$ events were stored by using Λ filter. The Λ filter was used in order to improve the generation efficiency and save disk space. The filter is based on the StMCfilter and requests at least one Λ or $\bar{\Lambda}$ in a pythia event. In the generation, we set PARP(90)=0.213 which is consistent with Embedding production of jet A_{LL} analysis by Kevin and K_factor = 2 which makes the p_{T} spectrum of Λ hyperons better consistent with data.

Jet Patch trigger conditions are applied using the standard STAR trigger simulator. Particle identification of p, π and Λ are implemented via StAssociateMaker in MC events then the same selection cuts are applied on except dE/dx. The efficiency of the track association is about 70% for single track and thus the eifficiency of finding a Λ into $p\pi$ is only 50%, which is an obstacle to generate MC sample with enough statistics. Jets are reconstructed with anti-K_{T} algorithm with $R = 0.6$ which is same with data.

5.2 Data and MC Comparison

The comparisons between data and MC were made. The $\Lambda\,(\bar{\Lambda})$ with p_{T} of $3 \sim 4\, GeV/c$ from JP1 sample are used as the example shown in the fillowing figures.

The comparison of primary vertex z after reweighting between data and simulation is shown in Fig. 5.2. The reweighting is made for ecah trigger sample separately. They are consistent with each other as the expected.

The comparisons of reconstructed variables for jet near-side Λ and $\bar{\Lambda}$ between data and simulation are shown in the following plots. The JP1 sample is used here for example and the others could be found from the link:
`http://www.star.bnl.gov/protected/spin/jcmei/pp200trans_2012/htmlCode/pp200trans_2012_MCDataComparison_J1.html`

Fig. 5.3 and Fig. 5.4 show the comparisons of the invariant mass, p_{T}, η, ϕ for jet near-side Λ and $\bar{\Lambda}$. In η comparison, data lower than simulation at the mid-rapidity is related to the efficiency drop in data from pileup. The MC smaple was produced uing pure pythia and pileup is not involved in.

Fig. 5.5 and Fig. 5.6 show the comparison of p_{T}, η, ϕ for p and π from jet near-side $\bar{\Lambda}$ and Λ. The similar behaviour can be found in η distribution.

The comparisons of selection cuts are shown in the following plots.

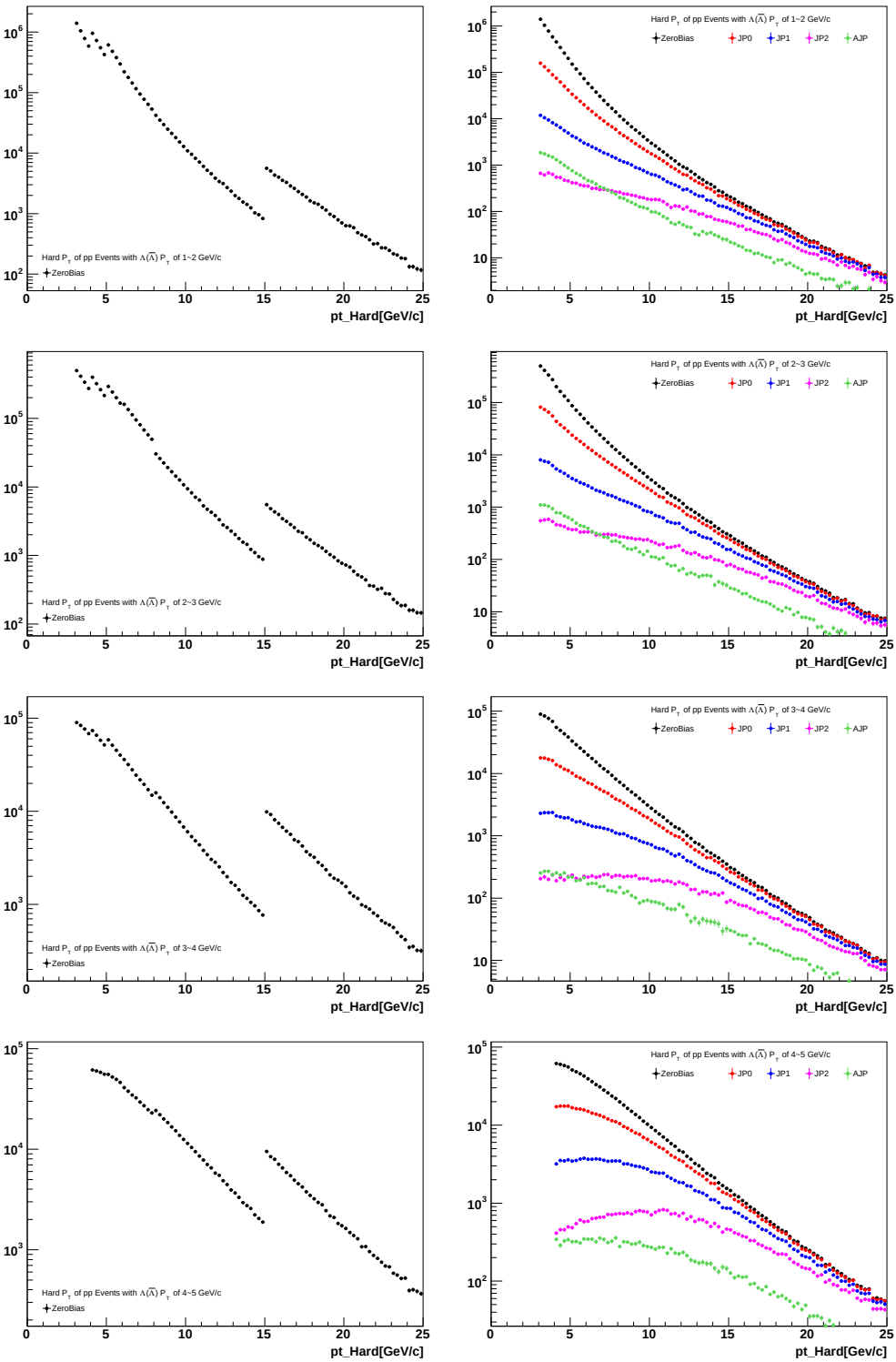

Figure 5.1: Hard Hard p_{T} distributions before (left) and affter (right) weighting for each of Λ p_{T} bins.

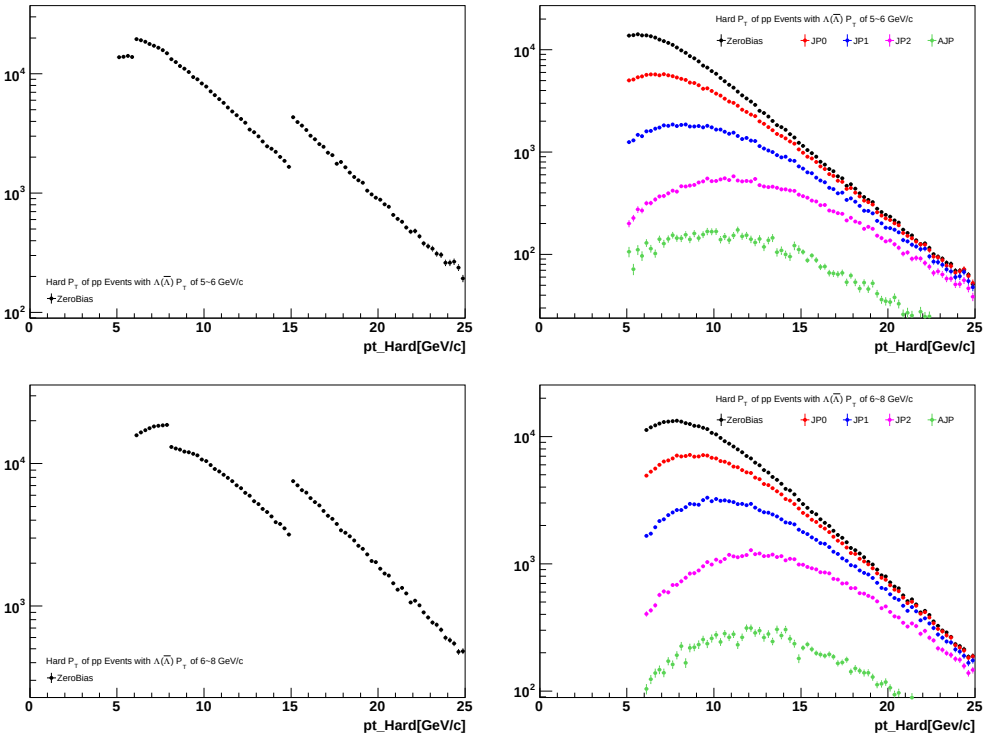

Figure 5.1: Hard p_{T} distribution before (left) and affter (right) weighting for each of Λ p_{T} bins.

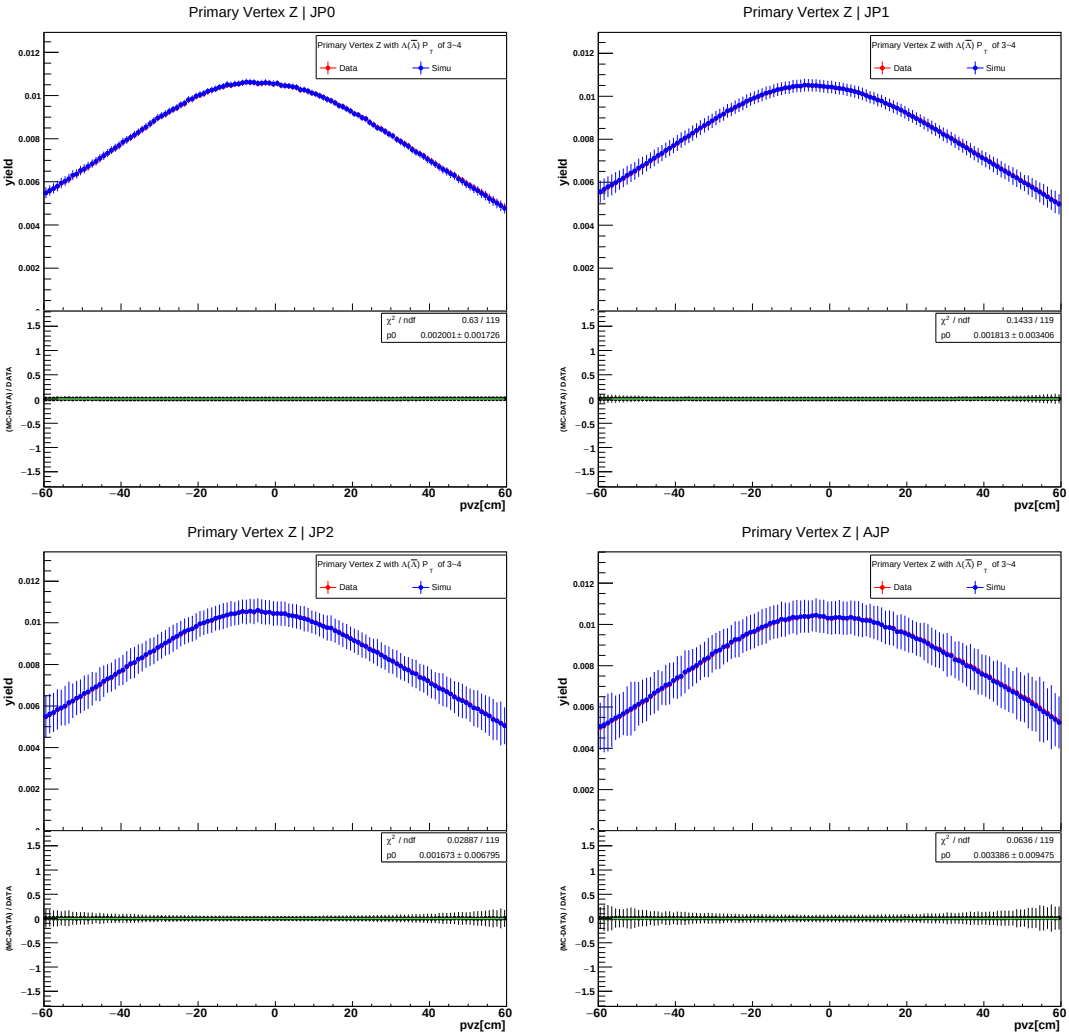

Figure 5.2: Comparison of primary vertex z after reweighting. The plots are for JP0, JP1, JP2, AJP trigger conditions from left to right in sequence.

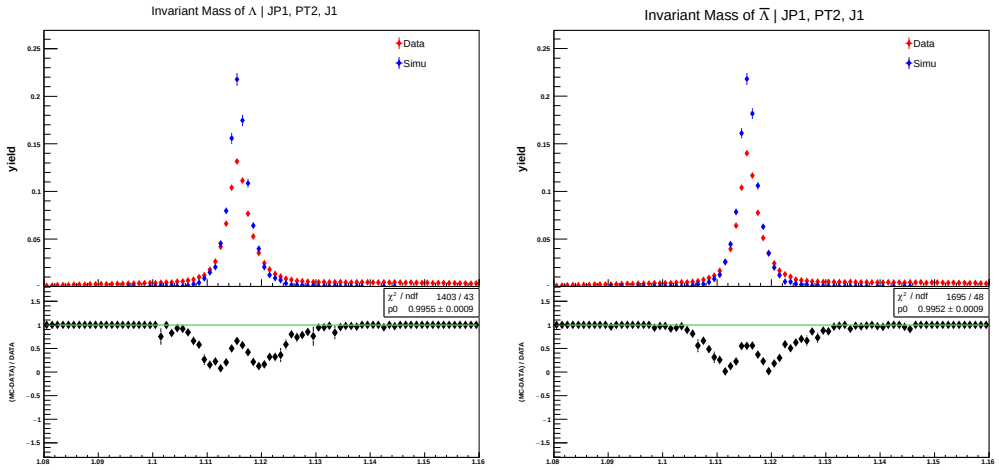

Figure 5.3: Comparison of reconstrcuted variables of $p\,(\bar{p})$ from jet near-side $\Lambda\,(\bar{\Lambda})$. The invariant mass of $\bar{\Lambda}$ are shown in the left panel and the right one is for Λ.

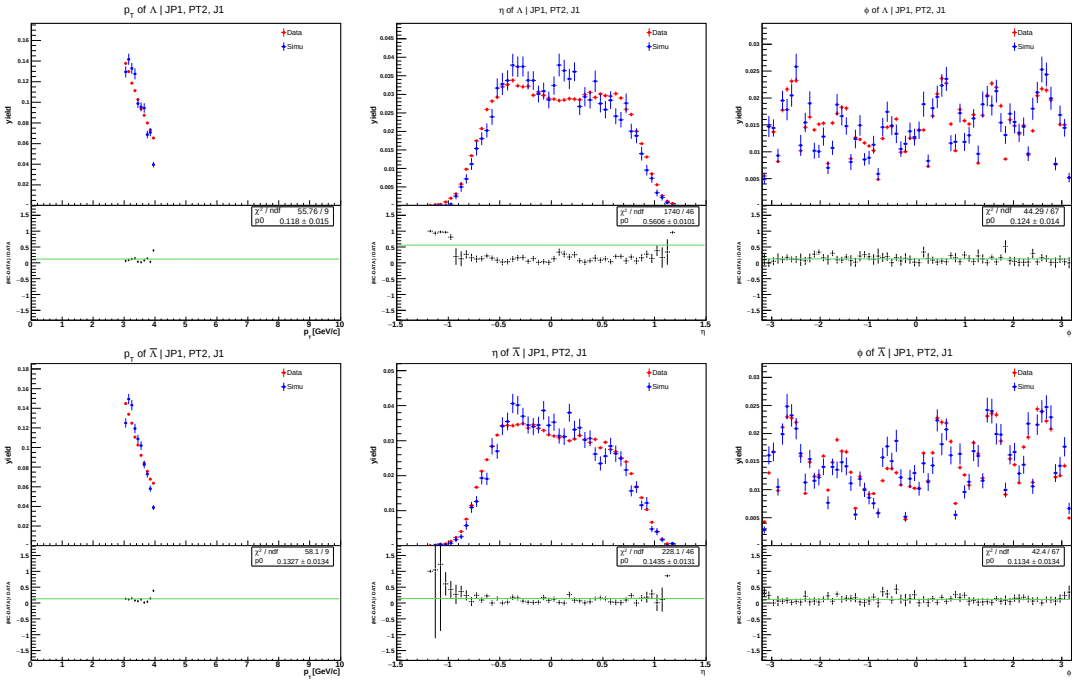

Figure 5.4: Comparison of reconstrcuted variables for jet near-side Λ and $\bar{\Lambda}$. The p_{T}, η, ϕ comparisons for Λ are shown in the upper panel and the lower panel is for $\bar{\Lambda}$.

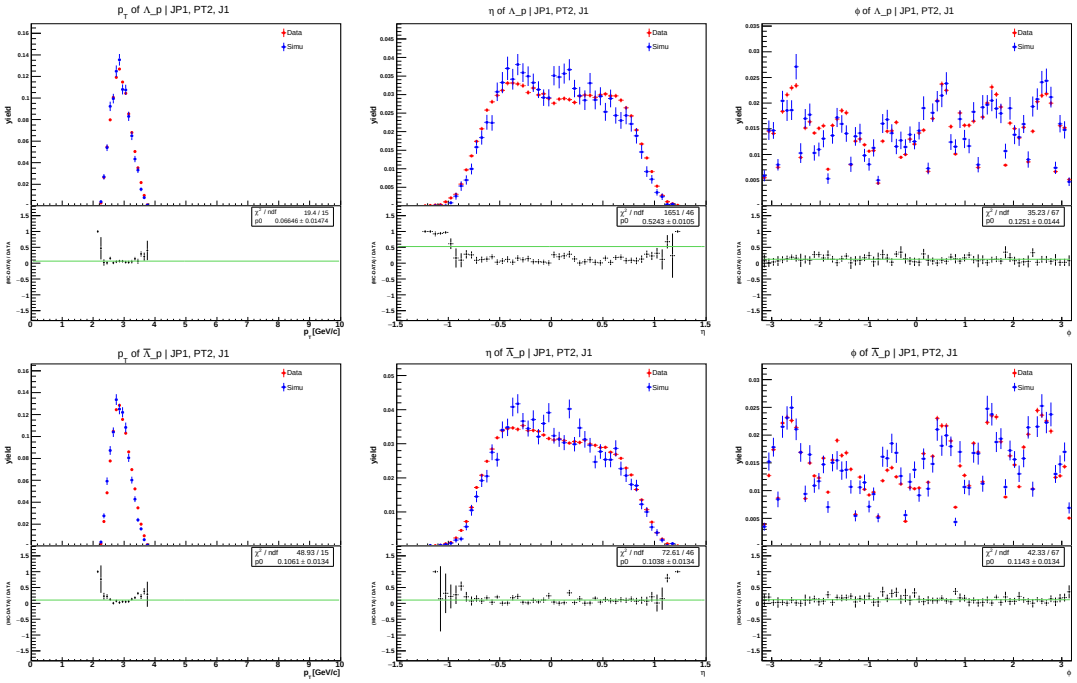

Figure 5.5: Comparisons of reconstrcuted variables of $p\,(\bar{p})$ from jet near-side $\Lambda\,(\bar{\Lambda})$. The p_{T}, η, ϕ comparisons for p from Λ are shown in the upper panel and the lower panel is for $\bar{p}$ from $\bar{\Lambda}$.

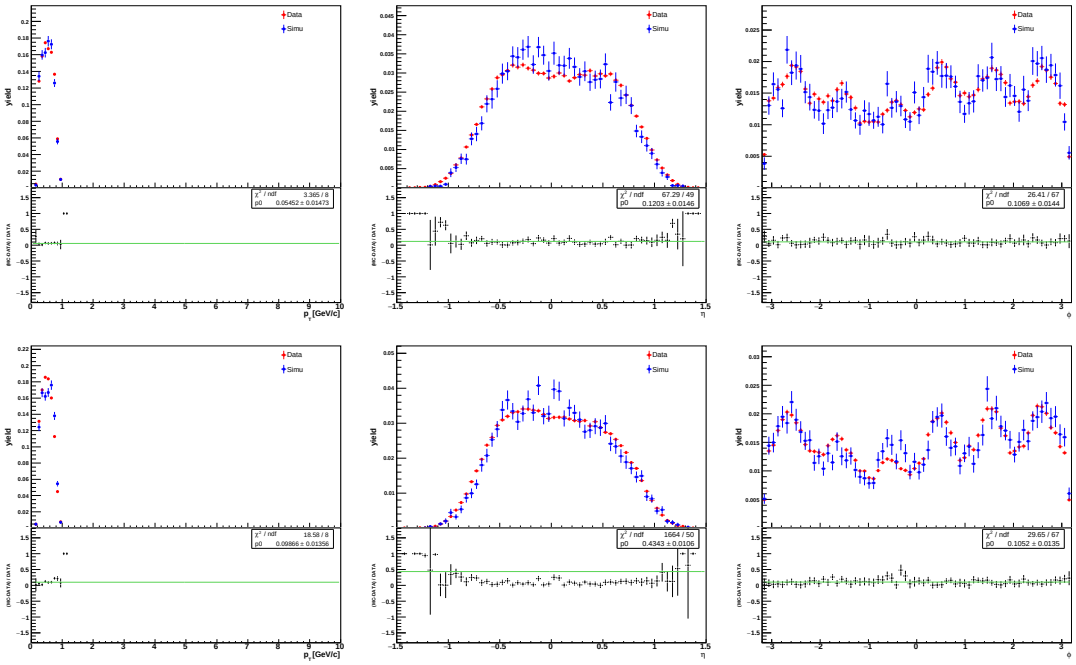

Figure 5.6: Comparisons of reconstrcuted variables for π^- (π^+) decay from jet near-side Λ ($\bar{\Lambda}$). The p_{T}, η, ϕ comparisons for π^- from Λ are shown in the upper panel and the lower panel is for π^+ from $\bar{\Lambda}$.

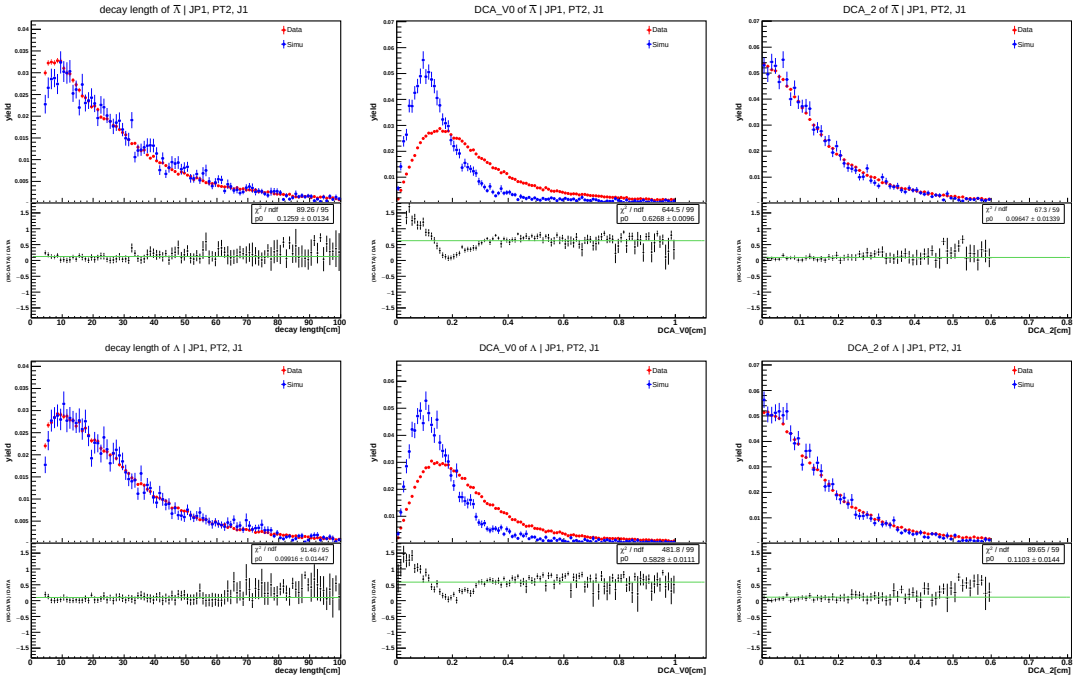

Figure 5.7: Comparisons of selection cuts for jet near-side Λ and $\bar{\Lambda}$. The decay length, DCA_V0, DCA_2 comparisons for Λ are shown in the upper panel and the lower panel is for $\bar{\Lambda}$.

Decay length, DCA_V0 and DCA_2 comparisons are shown in Fig. 5.7. Significant difference can be observed in DCA_V0 comparison. This is because the resolution of primary vertex in simulation is better than in data.

The comparisons of DCA_p and DCA_π are shown in Fig. 5.8.

The comparisons between data and simulation is generally consistent with each other.

In order to make sure whether the annihilation effect of $\bar{p}$ is simulated in the MC production, the ratio of $\bar{\Lambda}/\Lambda$ is studied in both simulation and data and the ratios for different classes of production are shown in Fig. 5.9. The natrual yield of $\bar{\Lambda}$ should be lower than Λ in pp collisions and the ratio is about 88% varying with p_{T} [1]. The ratios shown in Fig. 5.9 indicate that more $\bar{\Lambda}$ than Λ are reconstructed relatively in lower p_{T} bins. This is caused by the annihilation effect of $\bar{p}$ which makes it easier to pass the trigger threshold for the event including $\bar{\Lambda}$. With the increasing of p_{T}, the energy contributed from the annihilation of $\bar{p}$ is no longer the main fraction making the trigger fired so the ratio is going down.

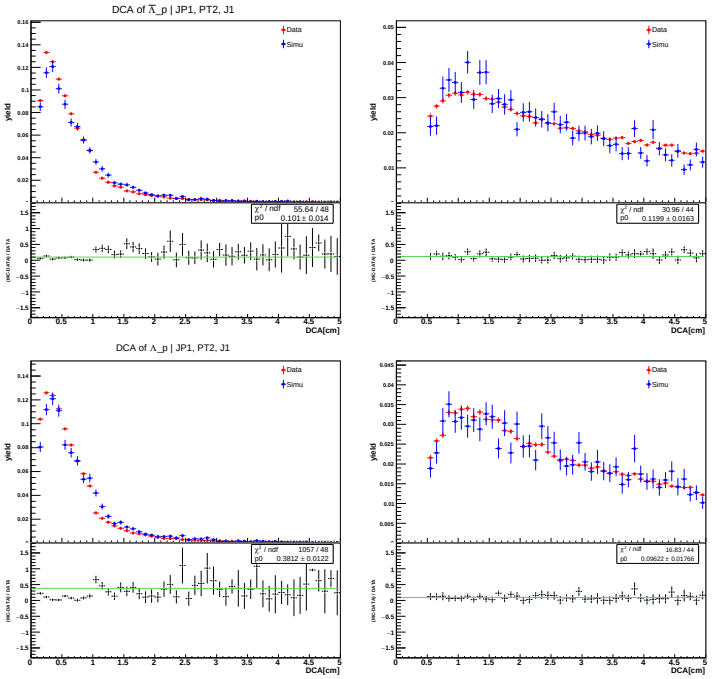

Figure 5.8: DCA of p, π from jet near-side Λ and $\bar{\Lambda}$. The upper panel is for Λ and the lower panel is for $\bar{\Lambda}$.

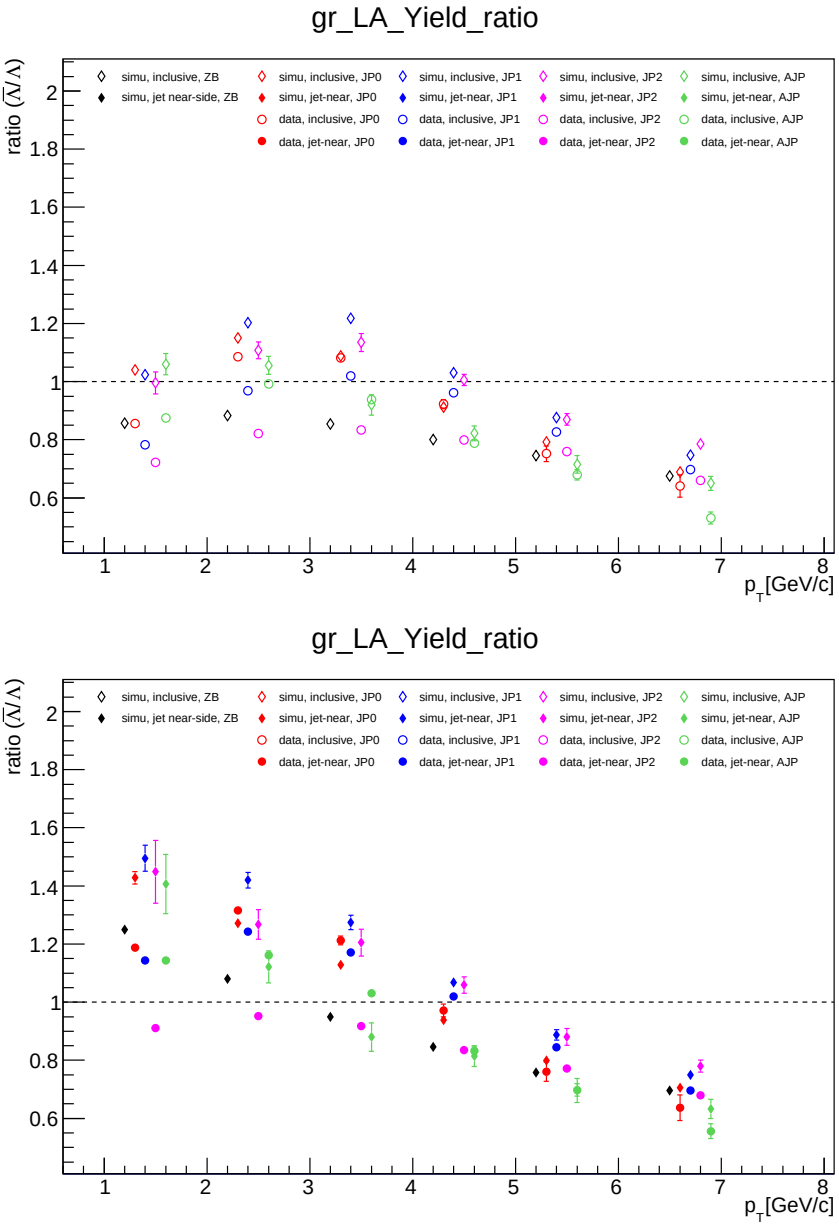

Figure 5.9: The ratio of $\bar{\Lambda}/\Lambda$ yield in different states. The left plot is for inclusive Λ and $\bar{\Lambda}$ and the right one is for the jet near-side Λ and $\bar{\Lambda}$.

6 Evaluation of Systematic Uncertainty

The systematic uncertainties in this analysis are stated in this section. Uncertainty sources we have considered include:

- the decay parameter,
- the measurement of beam polarization,
- the pileup effect,
- the estimation of residual background fraction,
- the trigger bias.

The systematic uncertainty caused by the trigger bias for the results of the combination sample was combined with weights determined by the point-by-point inverse statistical variance (as in an ordinary weighted average). The systematic scale uncertainties were reevaluated for the $D_{\rm TT}$ value of the combined sample. The systematic uncertainties from the estimation of the residual background fraction and pileup were reevaluated using the trigger combined sample.

6.1 Uncertainty from Decay parameter

The decay parameter α is taken from external measurements. We use the PDG value, 0.0642 ± 0.013 [4]. This 2% scale uncertainty is common to the JP trigger samples.

6.2 Uncertainty from Beam polariaztion

The magnitude of the beam polarizations is measured by the RHIC polarimetry group and has a 3.4% scale uncertainty for Run12 $\sqrt{s} = 100\,\text{GeV}$ data.

The beam polarization and its uncertainty are evaluated using the present data. The details of the measurement could be found from the link:
`http://public.bnl.gov/docs/cad/Documents/RHIC%20polarization%20for%20Runs%209-12.pdf` The uncertainty of this part is estimated via the scale multiply the $D_{\rm TT}$ mean value of the trigger-combined data sample.

6.3 Uncertainty from Estimation of Residual Background Fraction

The transverse spin transfer $D_{\rm TT}$ is extracted using Eq. 6.1 considering the background substraction.

$$D_{\rm TT} = \frac{D_{\rm TT}^{raw} - r D_{\rm TT}^{bkg}}{1 - r}, \tag{6.1}$$

where $D_{\rm TT}^{raw}$ is the $D_{\rm TT}$ value using the Λ candidates in the signal mass window containing residual backgrounds. The uncertainty in the residual background fraction is taken into account as a systematic uncertainty of $D_{\rm TT}$. The background fraction used in the main results is evaluated by counting events in the side-bands, interpolating them to the signal region, and comparing them with the observed counts in the signal region.

In order to estimate the systematic uncertainty caused by the background estimation, the background fraction was estimated also from a linear fit to the background and

Gaussian to describe the signal. The difference of the resulting $D_{\rm TT}$ values for these two methods is taken as the sysmatic uncertainty in r. The results are listed in TABLE. 6.1 with p_T for trigger combined data sample.

Table 6.1: Uncertainty to $D_{\rm TT}$ from estimation of residual background fraction for Λ and $\bar{\Lambda}$

	$0 < \eta < 1.2$		$-1.2 < \eta < 0$	
$p_{\rm T}$ [GeV/c]	Λ	$\bar{\Lambda}$	Λ	$\bar{\Lambda}$
$1 \sim 2$	0.0000	0.0000	0.0000	0.0000
$2 \sim 3$	0.0000	0.0000	0.0000	0.0000
$3 \sim 4$	0.0000	0.0000	0.0000	0.0000
$4 \sim 5$	0.0000	0.0001	0.0002	0.0004
$5 \sim 6$	0.0009	0.0001	0.0005	0.0003
$6 \sim 8$	0.0028	0.0002	0.0002	0.0007

6.4 Uncertainty from Pileup

The effect of event-overlap was studied by hyperon data sample and examining the hyperon yield per STAR event versus collision rate. The ratio is expected to be constant in the absednce of pile-up when the collision rate was 20 kHz. Constant and linear extrapolation to small collision rate, where pileup logically vanishes, was used to assess this systematic uncertainty contribution. The factor of pileup effect was estimated using the 4 JP samples and separately for the spin 4-bit sorted sample. Fig. 6.1 and Fig. 6.2 show the distribution for Λ and $\bar{\Lambda}$ of JP trigger combined sample.

The values are tabulated in TABLE. 6.2.

The systematic uncertainty propagation on $D_{\rm TT}$ due to pileup is calculated by determining the difference between the extracted $D_{\rm TT}$ sample and the pileup corrected $D_{\rm TT}$ for each spin 4-bit configuration,

$$(\delta D_{\rm TT}^{sys.pileup})^2 = \sum_{k=++,-+,+-,--} [D_{\rm TT}(n^k) - D_{\rm TT}((1-u^k)n^k)]^2, \qquad (6.2)$$

where n^{++}, n^{-+}, n^{+-}, and n^{--} are the spin 4-bit sorted hyperons counts and u^{++}, u^{-+}, u^{+-}, and u^{--} are the spin 4-bit sorted pileup contributions. The uncertainty values from pileup for trigger combined data sample are tabulated in TABLE. 6.3.

Table 6.2: Factors of pileup contribution for Λ and $\bar{\Lambda}$ for each spin configuration.

spin bit	5	6	9	10
Λ	0.087 ± 0.010	0.104 ± 0.011	0.084 ± 0.010	0.097 ± 0.011
$\bar{\Lambda}$	0.093 ± 0.010	0.076 ± 0.010	0.092 ± 0.010	0.088 ± 0.010

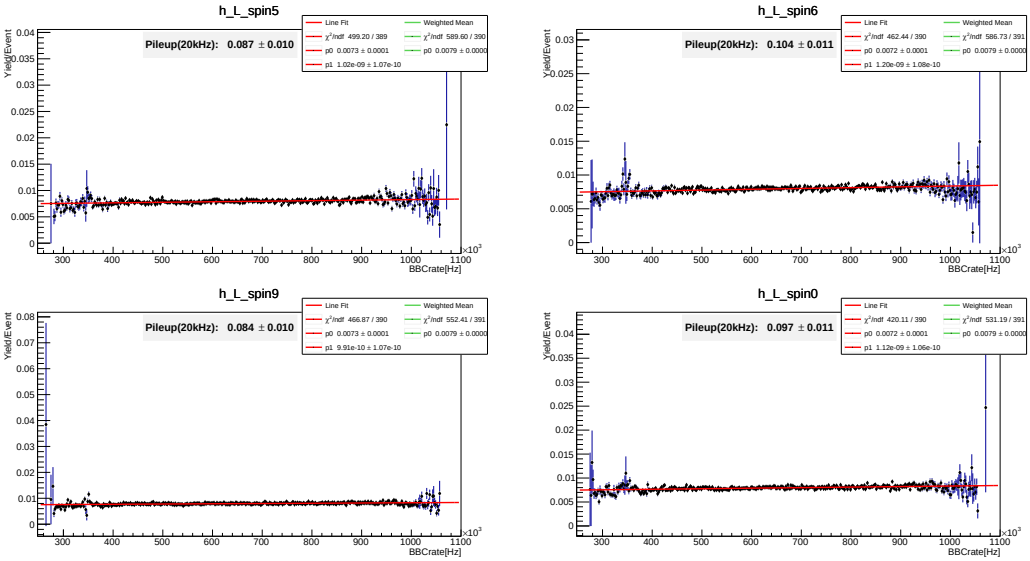

Figure 6.1: Hyperon yield vs. collision rate in spin 4-bit configurations of Λ for JP trigger combination. The upper-left graph is for spinbit-5, the upper right graph is for spinbit-6, the low left one is for spinbit-9 and the low right one is for spinbit-10.

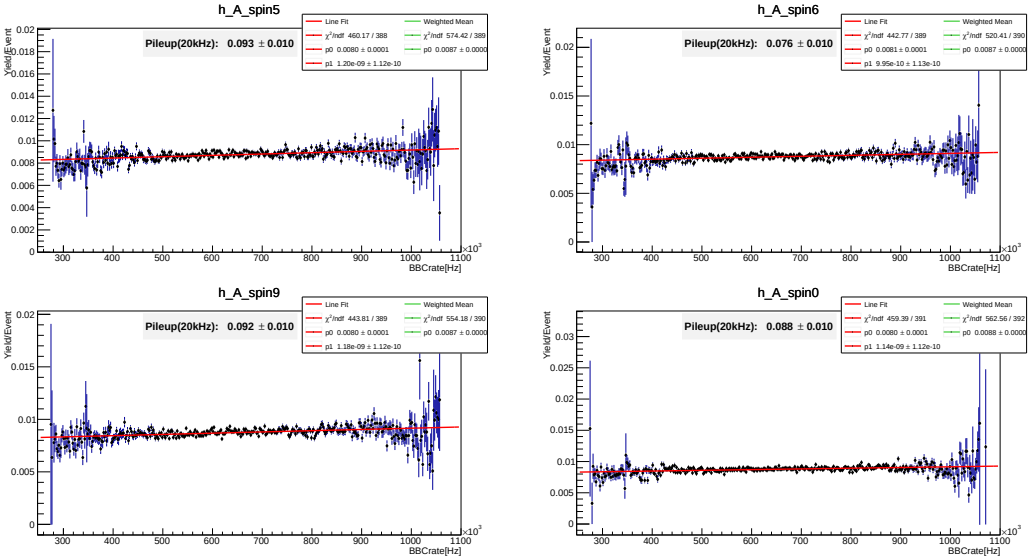

Figure 6.2: Hyperon yield vs. collision rate in spin 4-bit configurations of $\bar{\Lambda}$ for JP trigger combination. The upper-left graph is for spinbit-5, the upper right graph is for spinbit-6, the low left one is for spinbit-9 and the low right one is for spinbit-10.

Table 6.3: Uncertainty to D_{TT} from pileup for Λ and $\bar{\Lambda}$

	$0 < \eta < 1.2$		$-1.2 < \eta < 0$	
p_{T} [GeV/c]	Λ	$\bar{\Lambda}$	Λ	$\bar{\Lambda}$
$1 \sim 2$	0.0005	0.0001	0.0006	0.0003
$2 \sim 3$	0.0002	0.0005	0.0007	0.0003
$3 \sim 4$	0.0002	0.0007	0.0002	0.0011
$4 \sim 5$	0.0017	0.0012	0.0014	0.0007
$5 \sim 6$	0.0013	0.0016	0.0013	0.0012
$6 \sim 8$	0.0009	0.0022	0.0017	0.0031

6.5 Uncertainty from Trigger Bias

The data samples in this analysis are triggered for energy deposits in BEMC and EEMC, but not directly on the Λ and $\bar{\Lambda}$. The trigger condition may thus introduce a bias that needs to be taken into account in either the measurement or the phenomenological interpretation of the data. We choose to account for the possible size of this effect in a systematic uncertainty in the measurements and have considered three main manifestations:

- changes in the fractional momentum z of the produced Λ and $\bar{\Lambda}$ within the associated jet,
- changes in the relative contributions from different hard sub-processes and fragmenting partons with different flavors in the production.
- possible differences in the fraction of feed-down contributions,

The uncertainty caused by each of the three items is estimated in each of the JP trigger data samples separately, then combined using ratios of each of the JP trigger data samples extracted in data as weights. For the trigger combined data sample, the uncertaintues of the three items are added in quadrature.

These possible changes are examined in MC simulation before and after applying the Jet Patch trigger conditions using the standard STAR trigger simulator and GEANT-based simulation framework. Events were produced using PYTHIA version 6.4.28 [6] with Perugia 2012 tune [7].

Theoretical model [8] is used to evaluate the uncertainty into D_{TT} from trigger bias. The polarization of hyperons is separated into two parts as shown in Eq. 6.3.

$$P_{H_i} = \sum_f t^F_{H_i,f} P_f R_{H_i,f} + \sum_j t^D_{H_i,H_j} P_{H_j} R_{H_i,H_j}, \tag{6.3}$$

The polarization of H_i hyperon is the sum of the polarization of H_i produced directly from the fragmenting parton and produced from other particle (H_j) decay. The first part shows the polarization of hyperons produced directly from fragmenting parton, where $t^F_{H_i,f}$ is the transfer of polarization from the fragmenting parton to final state

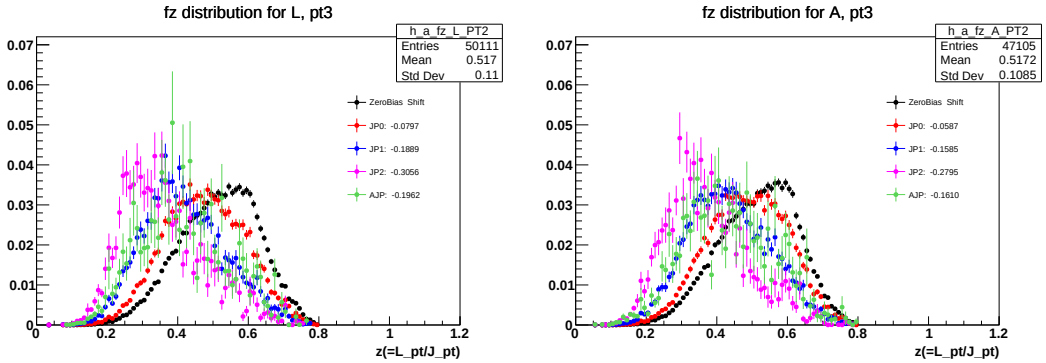

Figure 6.3: z distribution for Λ (in the left) and $\bar{\Lambda}$ (in the right) with p_{T} of $3 \sim 4\,\mathrm{GeV}/c$. X aixs shows z and Y axis shows the yield after normalized. The shifts of the mean values related to the mean value of zero bias sample are shown in the legend.

hypreons directly, P_f is the polarization of the fragmenting parton and $R_{H_i,f}$ is the relative fraction of H_i produced directly from fragmenting parton; The second part is about the polarization of H_i produced from other hyperons decay and $t^D_{H_i,H_j}$ is the transfer of polarization from other polarized hyperons.

6.5.1 Fractional momentum z

The fractional momentum z is defined as the ratio of p_{T}^{Λ} over $p_{\mathrm{T}}^{jet.asso}$, namely

$$z = \frac{p_{\mathrm{T}}^{\Lambda}}{p_{\mathrm{T}}^{jet.accosiated}} \tag{6.4}$$

It can be changed with JP trigger condition applied and the D_{TT} is dependent on z based on the model calculation. z are extracted from the MC sample before and after applying JP trigger conditions and shown in Fig. 6.3.

The z-dependent D_{TT} for Λ and $\bar{\Lambda}$ calculated using the model are shown in Fig. 6.4.

The D_{TT} values are corresponding to z for each trigger are obtained using Eq. 6.5,

$$D_{\mathrm{TT}} = \frac{\sum_i D^i_{\mathrm{TT}} n^i}{\sum_i n^i}, \tag{6.5}$$

where n^i and D^i_{TT} are the number of Λ or $\bar{\Lambda}$ offered by the MC sample and the value of D_{TT} calculated using the model in the ith bin along z. We assigned the D_{TT} value of the last bin in the D_{TT} versus z to the *bins* with $z > 0.85$ and the events in the bins with $z > 1.0$ are excluded in the calculation.

The differences of D_{TT} between before and after applying the triger conditions are used as the systematic uncertainty to D_{TT} form z shift. The uncertainty is shown in TABLE. 6.4

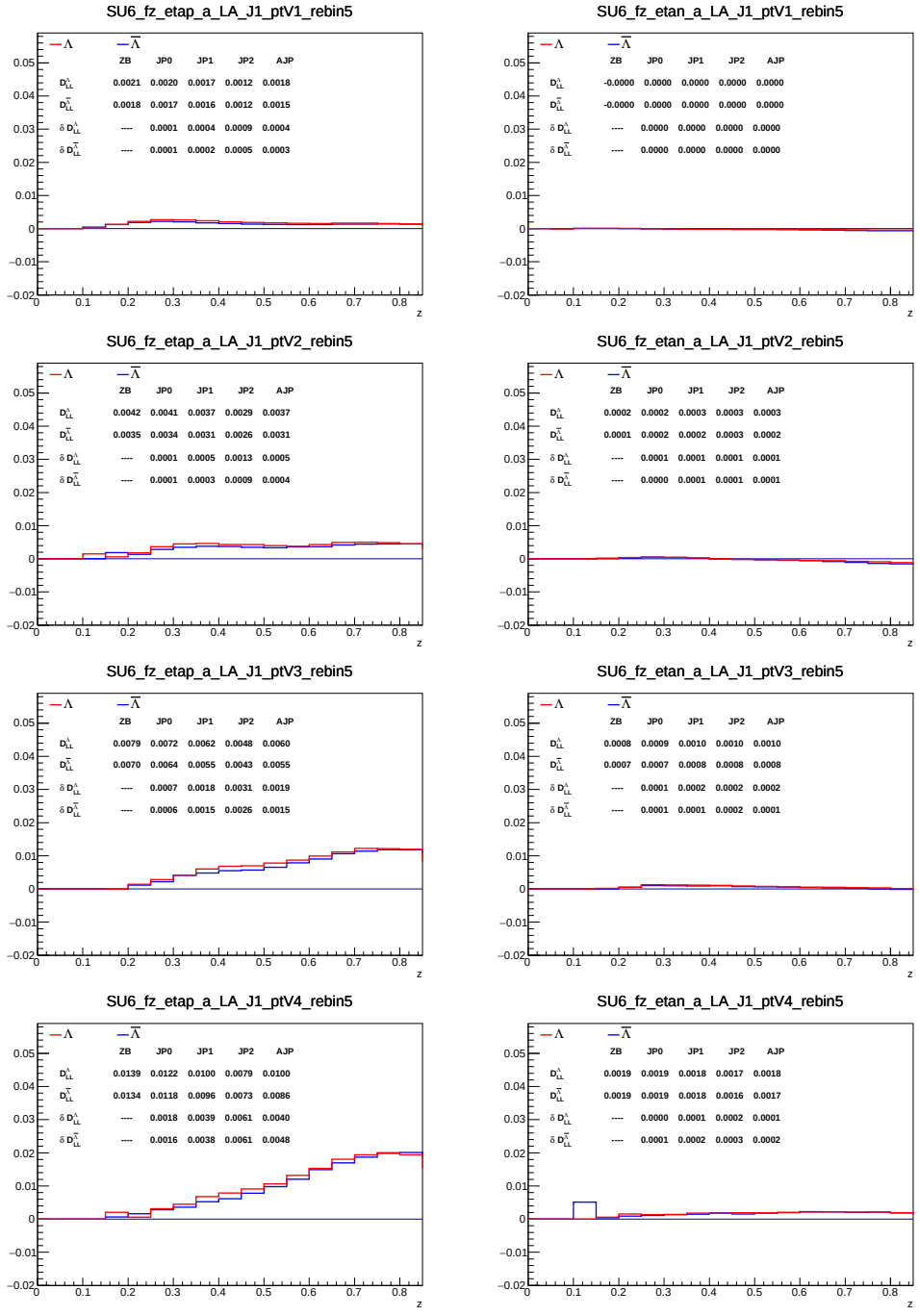

Figure 6.4: D_{TT} for Λ and $\bar{\Lambda}$ versus z calculated using the model in different p_{T} bins with positive η (left) and negative η (right).

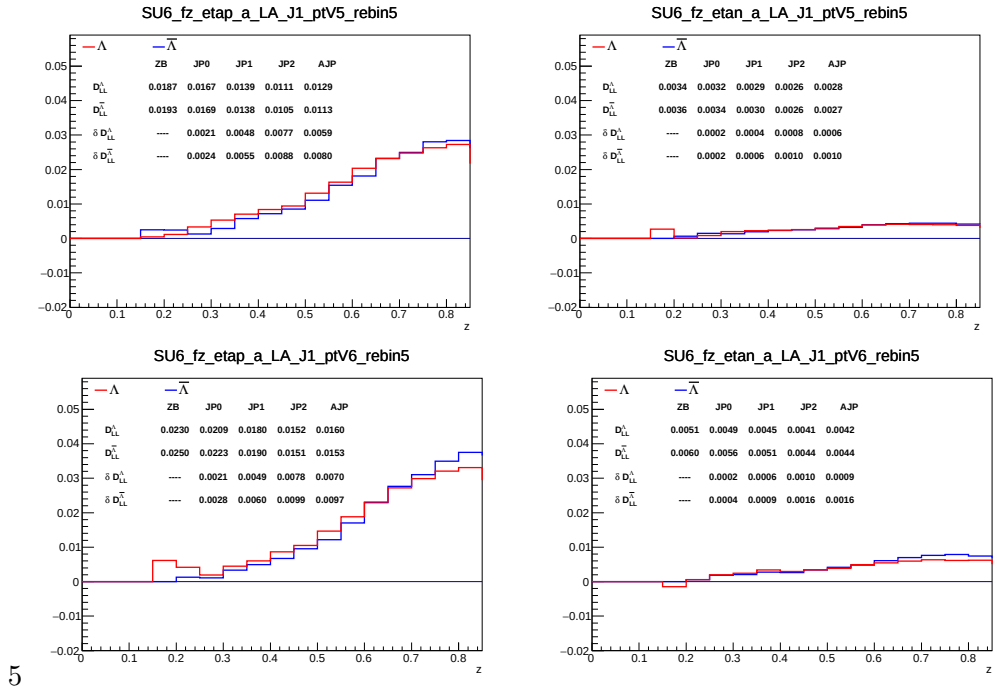

Figure 6.4: D_{TT} for Λ and $\bar{\Lambda}$ versus z calculated using the model in different p_{T} bins with positive η (left) and negative η (right).

Table 6.4: Uncertainty to D_{TT} from z shift for Λ and $\bar{\Lambda}$

$0 < \eta < 1.2$										
	JP0		JP1		JP2		AJP		Combined	
p_{T}	Λ	$\bar{\Lambda}$	Λ	$\bar{\Lambda}$	Λ	$\bar{\Lambda}$	Λ	$\bar{\Lambda}$	Λ	$\bar{\Lambda}$
$1 \sim 2$	0.0001	0.0001	0.0004	0.0002	0.0009	0.0005	0.0004	0.0003	0.0005	0.0003
$2 \sim 3$	0.0001	0.0001	0.0005	0.0003	0.0013	0.0009	0.0005	0.0004	0.0007	0.0004
$3 \sim 4$	0.0007	0.0006	0.0018	0.0015	0.0031	0.0026	0.0019	0.0015	0.0021	0.0017
$4 \sim 5$	0.0018	0.0016	0.0039	0.0038	0.0061	0.0061	0.0040	0.0048	0.0045	0.0044
$5 \sim 6$	0.0021	0.0024	0.0048	0.0055	0.0077	0.0088	0.0059	0.0080	0.0058	0.0067
$6 \sim 8$	0.0021	0.0028	0.0049	0.0060	0.0078	0.0099	0.0070	0.0097	0.0061	0.0077
$-1.2 < \eta < 0$										
	JP0		JP1		JP2		AJP		Combined	
p_{T}	Λ	$\bar{\Lambda}$	Λ	$\bar{\Lambda}$	Λ	$\bar{\Lambda}$	Λ	$\bar{\Lambda}$	Λ	$\bar{\Lambda}$
$1 \sim 2$	0.0000	0.0000	0.0000	0.0000	0.0000	0.0000	0.0000	0.0000	0.0000	0.0000
$2 \sim 3$	0.0001	0.0000	0.0001	0.0001	0.0001	0.0001	0.0001	0.0001	0.0001	0.0001
$3 \sim 4$	0.0001	0.0001	0.0002	0.0001	0.0002	0.0002	0.0002	0.0001	0.0002	0.0001
$4 \sim 5$	0.0000	0.0001	0.0001	0.0002	0.0002	0.0003	0.0001	0.0002	0.0001	0.0002
$5 \sim 6$	0.0002	0.0002	0.0004	0.0006	0.0008	0.0010	0.0006	0.0010	0.0006	0.0008
$6 \sim 8$	0.0002	0.0004	0.0006	0.0009	0.0010	0.0016	0.0009	0.0016	0.0008	0.0012

6.5.2 Subprocess & flavor of fragmenting parton

The polarization of the fragmenting parton is transfed from the incoming parton which can be expressed as

$$P_f = \frac{\delta f}{f} D_T^{a^\uparrow b \to c^\uparrow d}, \tag{6.6}$$

where P_c is the polarization of the fragmenting parton c, δf is the transversely polarized partonic distribution function and f is the unpolaried partonic distribution function and $D_T^{a^\uparrow b \to c^\uparrow d}$ is the partonic spin transfer for the subprocess $a^\uparrow b \to c^\uparrow d$. The JP trigger conditions could change the relative fractions of different subprocess and thus the relative fractions of the fragmenting partons with different flavor. The relative fractions of the subprocess are obtained from the MC sample and the example of p_{T} of $3 \sim 4\,\mathrm{GeV/c}$ is shown in Fig. 6.5. The main subprocesses are $q_a q_b \to q_a q_b$, $q_a g \to q_a g$ and $gg \to gg$.

The relative fractions for all p_{T} bins are summaried in Fig. 6.6. The relative fractions of $qq \to qq$ and $qg \to qg$ are increasing and the relative fraction of $gg \to gg$ is decreasing with the trigger threshold increasing and hyperon p_{T} increasing.

The relative fractions of the fragmenting partons with different flavors changed with the different trigger conditions applied. The relative fractions are extracted from the MC sample. Fig. 6.7 shows the original fragmenting parton flavors for $\Lambda\,(\bar{\Lambda})$ with p_{T} of $3 \sim 4\,\mathrm{GeV/c}$ as an example. The fraction distribution indicates that gluon is the main part in the fragmenting partons for both of Λ and $\bar{\Lambda}$ and d and u quarks are following. The $\bar{s}$ quark is obviously a main source for $\bar{\Lambda}$ than Λ. This is also the reason why we expect $\bar{\Lambda}$ is able to provide information for the polarization of strange sea quark.

The relative fractions for all p_{T} bins are summaried in Fig. 6.8. The relative fraction of gluon is decreasing while the relative fractions of quarks are increasing with hyperon p_{T} increasing. With trigger threshold increasing, the relative fraction of $s\,(\bar{s})$ is decreasing while the relative fractions of gluon, $d\,(\bar{d})$ and $u\,(\bar{u})$ are increasing.

The relative fraction changes of subprocess and fragmenting parton with different flavor is combined to each other strongly. In the model calculation, the relative fraction of fragmenting parton with different flavor is used as the input to calculate the D_{TT} for each trigger. Based on the model calculation and the relative fractions of fragmenting parton with different flavor, the trigger-dependent D_{TT} was obtained. The difference of D_{TT} between before and after applying the trigger conditions is used as the systematic uncertainty to D_{TT} from the changes of subprocess and fragmenting parton flavor. The uncertainty from this part is tabulated in TABLE. 6.5.

6.5.3 Feed-down contributions

The possible effect from differences in the feed-down contribution on Λ and $\bar{\Lambda}$ production were studied in simulation. The relative fractions of $\Lambda\,(\bar{\Lambda})$'s mother particles can be obtained from the MC data samples.

The relative fractions for all p_{T} bins are summaried in Fig. 6.9. The solid circle is representative of the hyperon produced directly from the fragmenting parton and this part is decreasing with trigger threshold increasing. The relative fractions of hyperons

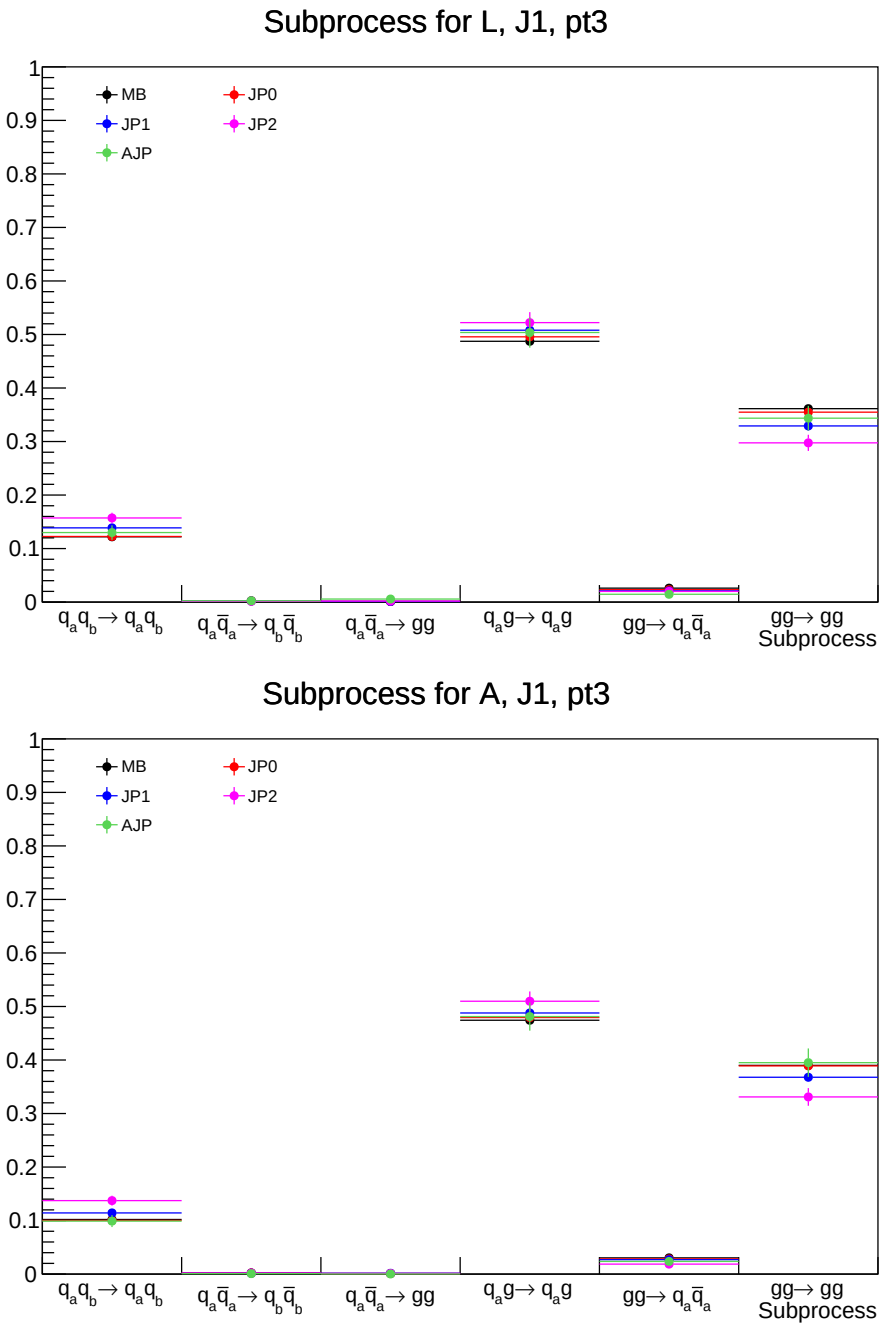

Figure 6.5: The relative fractions of subprocess for Λ (upper panel) and $\bar{\Lambda}$ (lower panel) with p_{T} of $3 \sim 4\,\mathrm{GeV/c}$.

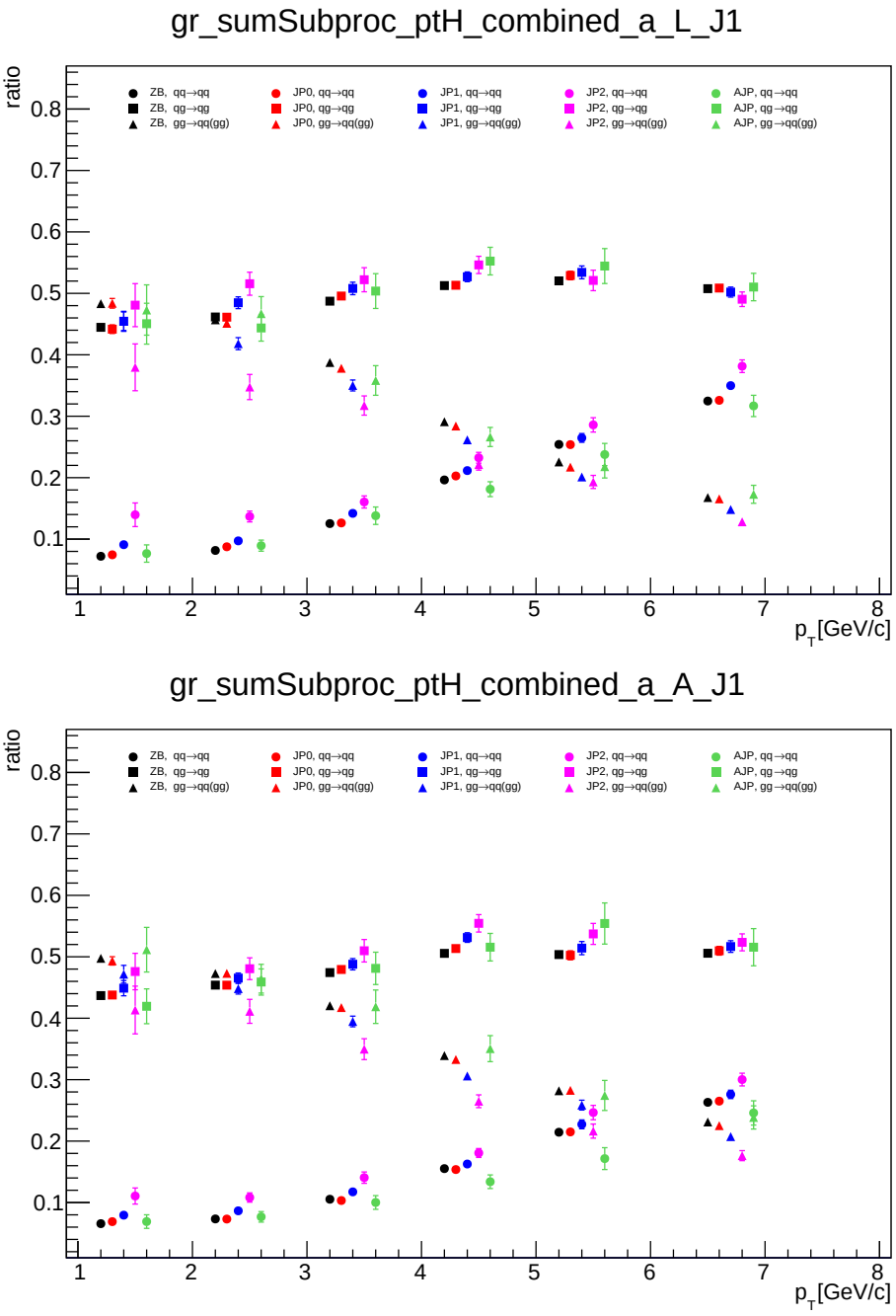

Figure 6.6: The relative fractions of subprocess for Λ (upper panel) and $\bar{\Lambda}$ (lower panel) in all p_{T} bins.

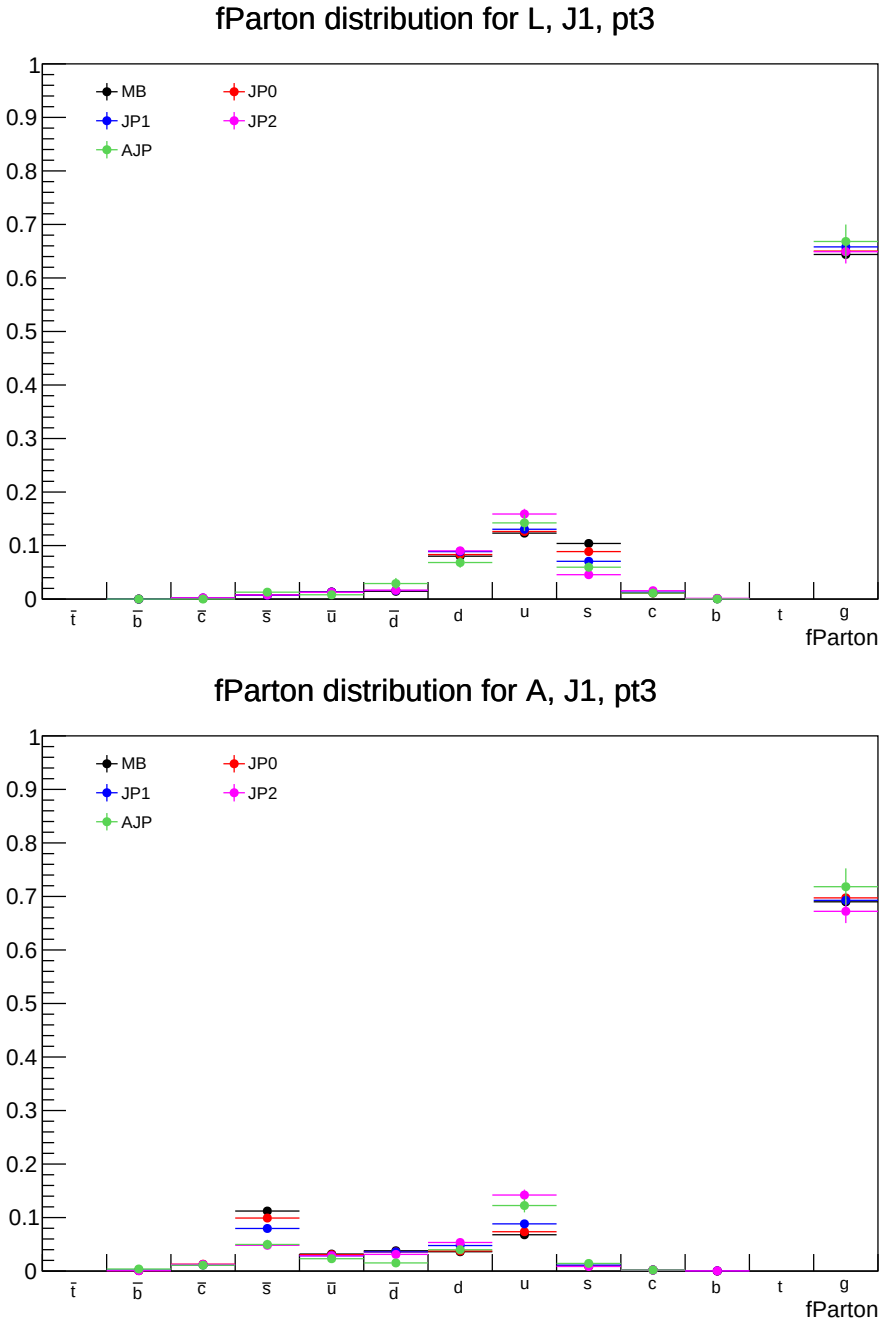

Figure 6.7: The relative fractions of fragmenting parton flavors for Λ (upper panel) and $\bar{\Lambda}$ (lower panel) with p_{T} of $3 \sim 4\,\mathrm{GeV/c}$.

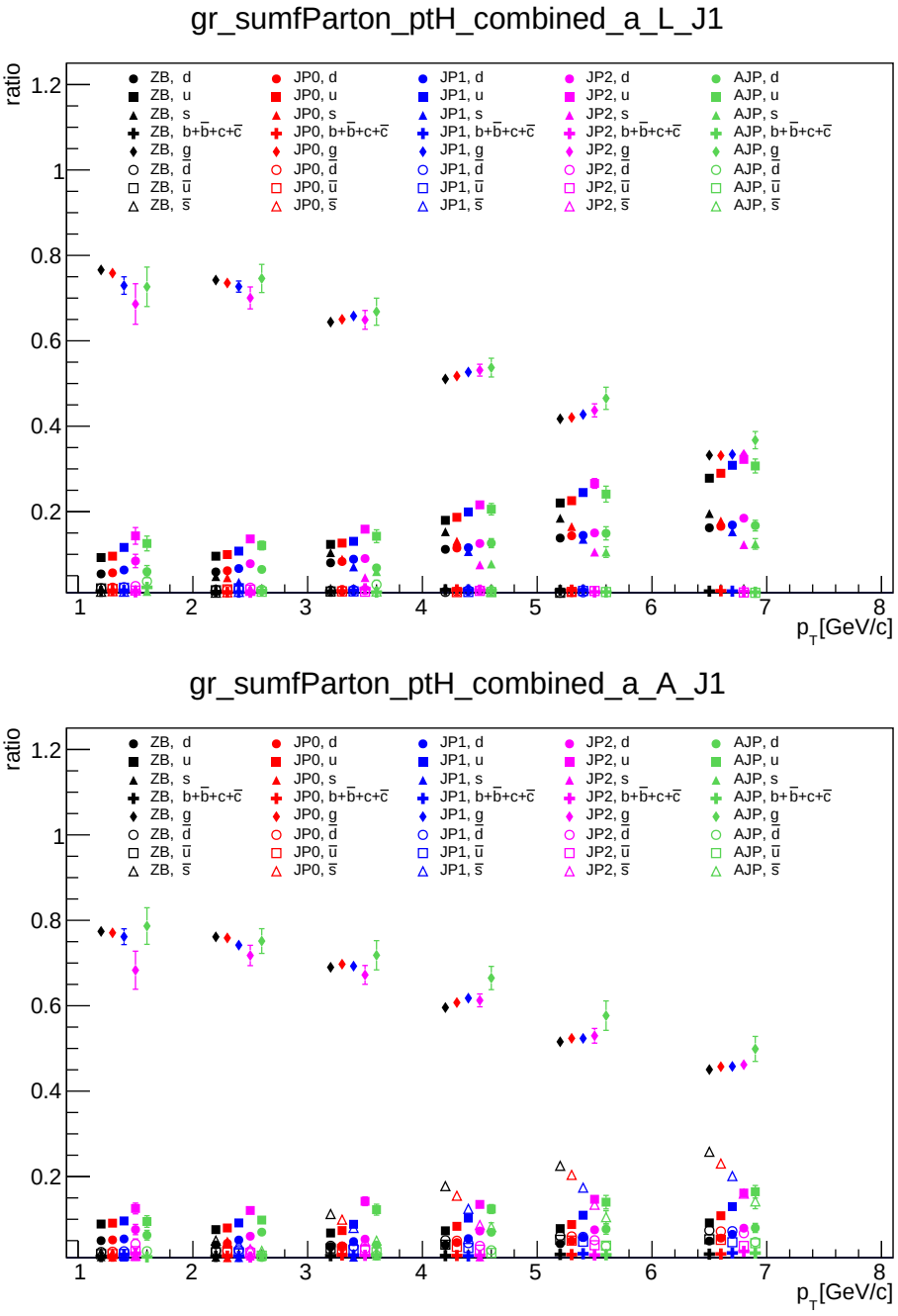

Figure 6.8: The relative fractions of fragmentin parton flavors for Λ (upper panel) and $\bar{\Lambda}$ (lower panel) in all p_{T} bins.

Table 6.5: Uncertainty to D_{TT} from subprocess & fragmenting parton flavor for Λ and $\bar{\Lambda}$

$0 < \eta < 1.2$										
	JP0		JP1		JP2		AJP		Combined	
p_{T}	Λ	$\bar{\Lambda}$	Λ	$\bar{\Lambda}$	Λ	$\bar{\Lambda}$	Λ	$\bar{\Lambda}$	Λ	$\bar{\Lambda}$
$1 \sim 2$	0.0000	0.0001	0.0002	0.0001	0.0003	0.0004	0.0003	0.0004	0.0002	0.0002
$2 \sim 3$	0.0001	0.0001	0.0005	0.0003	0.0011	0.0007	0.0009	0.0001	0.0007	0.0004
$3 \sim 4$	0.0005	0.0002	0.0013	0.0006	0.0023	0.0017	0.0014	0.0005	0.0015	0.0009
$4 \sim 5$	0.0011	0.0003	0.0024	0.0009	0.0043	0.0021	0.0041	0.0007	0.0031	0.0012
$5 \sim 6$	0.0011	0.0005	0.0029	0.0013	0.0048	0.0019	0.0046	0.0023	0.0037	0.0016
$6 \sim 8$	0.0011	0.0006	0.0026	0.0013	0.0048	0.0022	0.0041	0.0019	0.0036	0.0017
$-1.2 < \eta < 0$										
	JP0		JP1		JP2		AJP		Combined	
p_{T}	Λ	$\bar{\Lambda}$	Λ	$\bar{\Lambda}$	Λ	$\bar{\Lambda}$	Λ	$\bar{\Lambda}$	Λ	$\bar{\Lambda}$
$1 \sim 2$	0.0000	0.0000	0.0000	0.0000	0.0000	0.0000	0.0000	0.0000	0.0000	0.0000
$2 \sim 3$	0.0000	0.0000	0.0000	0.0001	0.0000	0.0001	0.0000	0.0000	0.0000	0.0001
$3 \sim 4$	0.0000	0.0000	0.0001	0.0000	0.0002	0.0001	0.0001	0.0000	0.0001	0.0000
$4 \sim 5$	0.0001	0.0001	0.0003	0.0002	0.0005	0.0003	0.0005	0.0001	0.0004	0.0002
$5 \sim 6$	0.0002	0.0001	0.0006	0.0003	0.0009	0.0004	0.0009	0.0005	0.0007	0.0003
$6 \sim 8$	0.0003	0.0002	0.0007	0.0004	0.0012	0.0006	0.0011	0.0006	0.0009	0.0005

produced from Σ^0, Σ^{*0} and Ξ^0 decay are increasing with the trigger threshold increasing. This is because that π^0 or γ is produced simultaneously in the decay, which provides more energy to make the trigger fired esaier.

Based on the model calculation and the relative fractions of feed-down sources for each trigger condition, the trigger-dependent D_{TT} was obtained. The difference of D_{TT} between before and after applying the trigger conditions is used as the systematic uncettainty to D_{TT} from the changes of the feed-down sources. TABLE. 6.6 shows the values of the uncertainty.

6.6 Total Systematic Uncertainty

The total systematic uncertainty was estimated by adding the above contributions in quadrature for each p_{T} interval in the analysis. This was done separately for the Λ and $\bar{\Lambda}$ samples with positive and negative η ranges. The values are shown in TABLE. 6.7.

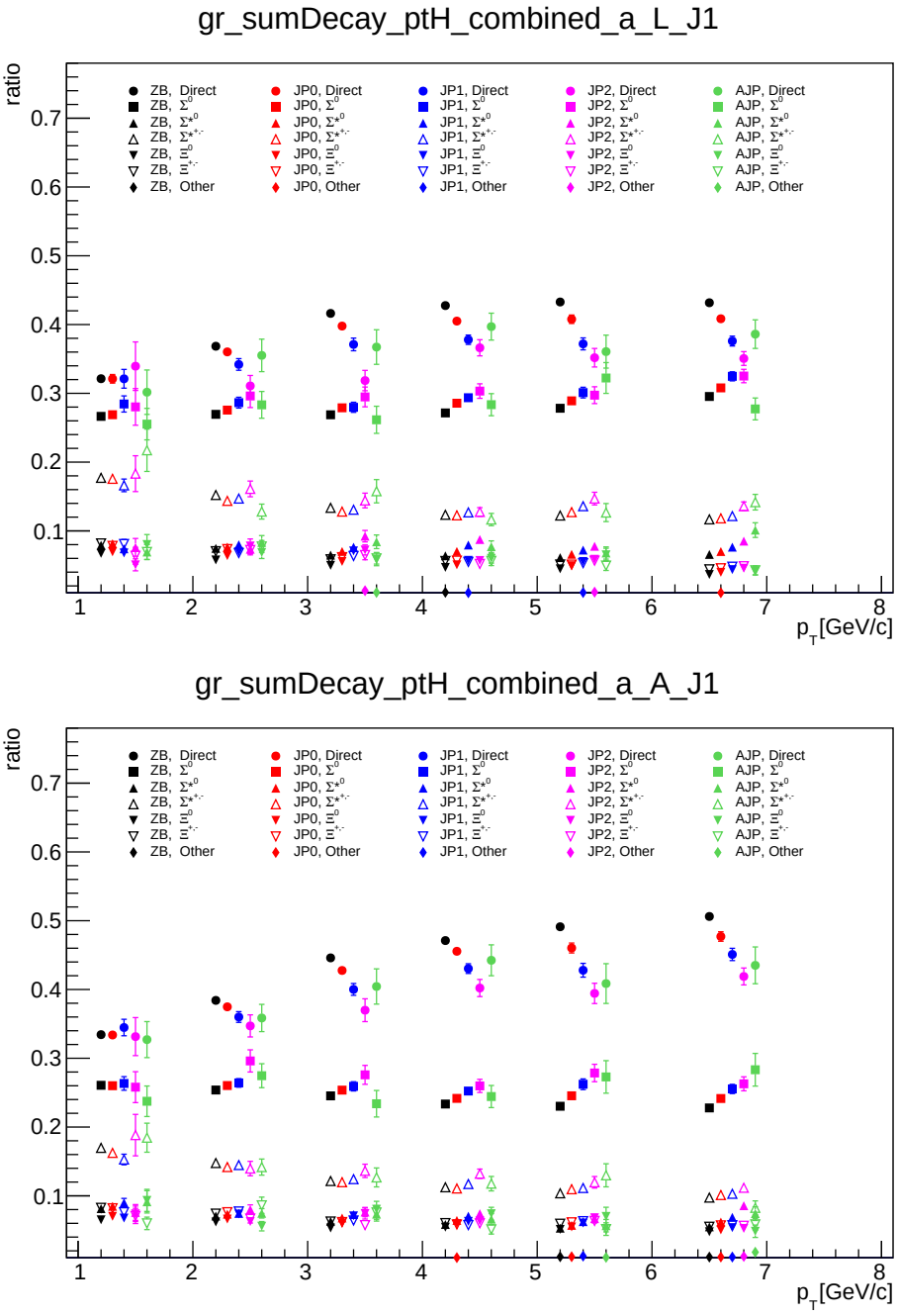

Figure 6.9: The feed-down fractions for Λ (upper panel) and $\bar{\Lambda}$ (lower panel) in all p_{T} bins.

Table 6.6: Uncertainty to D_{TT} from feed-down for Λ and $\bar{\Lambda}$

$0 < \eta < 1.2$										
	JP0		JP1		JP2		AJP		Combined	
p_{T}	Λ	$\bar{\Lambda}$	Λ	$\bar{\Lambda}$	Λ	$\bar{\Lambda}$	Λ	$\bar{\Lambda}$	Λ	$\bar{\Lambda}$
$1 \sim 2$	0.0000	0.0001	0.0001	0.0001	0.0000	0.0001	0.0003	0.0001	0.0001	0.0001
$2 \sim 3$	0.0002	0.0000	0.0004	0.0001	0.0004	0.0003	0.0001	0.0000	0.0004	0.0001
$3 \sim 4$	0.0004	0.0002	0.0003	0.0003	0.0014	0.0008	0.0002	0.0004	0.0007	0.0004
$4 \sim 5$	0.0007	0.0003	0.0013	0.0007	0.0020	0.0013	0.0016	0.0005	0.0015	0.0008
$5 \sim 6$	0.0007	0.0008	0.0013	0.0014	0.0009	0.0024	0.0013	0.0030	0.0012	0.0018
$6 \sim 8$	0.0006	0.0010	0.0019	0.0019	0.0024	0.0028	0.0008	0.0020	0.0020	0.0022

$-1.2 < \eta < 0$										
	JP0		JP1		JP2		AJP		Combined	
p_{T}	Λ	$\bar{\Lambda}$	Λ	$\bar{\Lambda}$	Λ	$\bar{\Lambda}$	Λ	$\bar{\Lambda}$	Λ	$\bar{\Lambda}$
$1 \sim 2$	0.0000	0.0000	0.0000	0.0000	0.0000	0.0000	0.0001	0.0000	0.0000	0.0000
$2 \sim 3$	0.0000	0.0000	0.0000	0.0001	0.0001	0.0001	0.0001	0.0001	0.0001	0.0001
$3 \sim 4$	0.0001	0.0000	0.0001	0.0000	0.0001	0.0000	0.0002	0.0000	0.0001	0.0000
$4 \sim 5$	0.0001	0.0001	0.0001	0.0001	0.0001	0.0001	0.0000	0.0001	0.0001	0.0001
$5 \sim 6$	0.0001	0.0001	0.0003	0.0003	0.0004	0.0004	0.0006	0.0002	0.0004	0.0003
$6 \sim 8$	0.0003	0.0002	0.0006	0.0003	0.0006	0.0005	0.0002	0.0006	0.0006	0.0004

Table 6.7: Total Systematic Uncertainty

	$0 < \eta < 1.2$		$-1.2 < \eta < 0$	
p_{T} [GeV/c]	Λ	$\bar{\Lambda}$	Λ	$\bar{\Lambda}$
$1 \sim 2$	0.0008	0.0006	0.0000	0.0003
$2 \sim 3$	0.0012	0.0008	0.0001	0.0003
$3 \sim 4$	0.0029	0.0021	0.0003	0.0011
$4 \sim 5$	0.0059	0.0049	0.0004	0.0009
$5 \sim 6$	0.0071	0.0073	0.0010	0.0017
$6 \sim 8$	0.0080	0.0086	0.0013	0.0041

7 Final Results

Events that satisfy the JP trigger conditions were analyzed as separate samples. Events that satisfy two or more conditions were analyzed only as part of one of the JP samples to avoid double-counting (or correlation). The D_{TT} results are consistent with each other within uncertainty. The D_{TT} results using the combined sample were also extracted.

The final results are shonwn in Fig. 7.1 including statistical uncertainty(black lines) and the systematic uncertainty (grey bands). The values are listed in TABLE. 7.1.

Table 7.1: Values of D_{TT} extracted form trigger combined sample

$0 < \eta < 1.2$						
	Λ			$\bar{\Lambda}$		
p_{T} [GeV/c]	D_{TT}	stat.	sys.	D_{TT}	stat.	sys.
$1 \sim 2$	0.000	0.007	0.001	0.011	0.006	0.001
$2 \sim 3$	0.013	0.008	0.001	-0.002	0.008	0.001
$3 \sim 4$	0.026	0.011	0.003	-0.002	0.011	0.002
$4 \sim 5$	-0.008	0.017	0.006	0.024	0.017	0.005
$5 \sim 6$	0.007	0.026	0.007	0.009	0.028	0.007
$6 \sim 8$	0.031	0.033	0.008	-0.034	0.040	0.009

$-1.2 < \eta < 0$						
	Λ			$\bar{\Lambda}$		
p_{T} [GeV/c]	D_{TT}	stat.	sys.	D_{TT}	stat.	sys.
$1 \sim 2$	-0.005	0.007	0.001	-0.001	0.006	0.000
$2 \sim 3$	-0.006	0.008	0.001	0.001	0.008	0.000
$3 \sim 4$	-0.017	0.011	0.001	-0.004	0.011	0.001
$4 \sim 5$	-0.023	0.017	0.002	0.002	0.017	0.001
$5 \sim 6$	0.023	0.026	0.002	0.017	0.028	0.002
$6 \sim 8$	0.021	0.033	0.002	-0.056	0.040	0.004

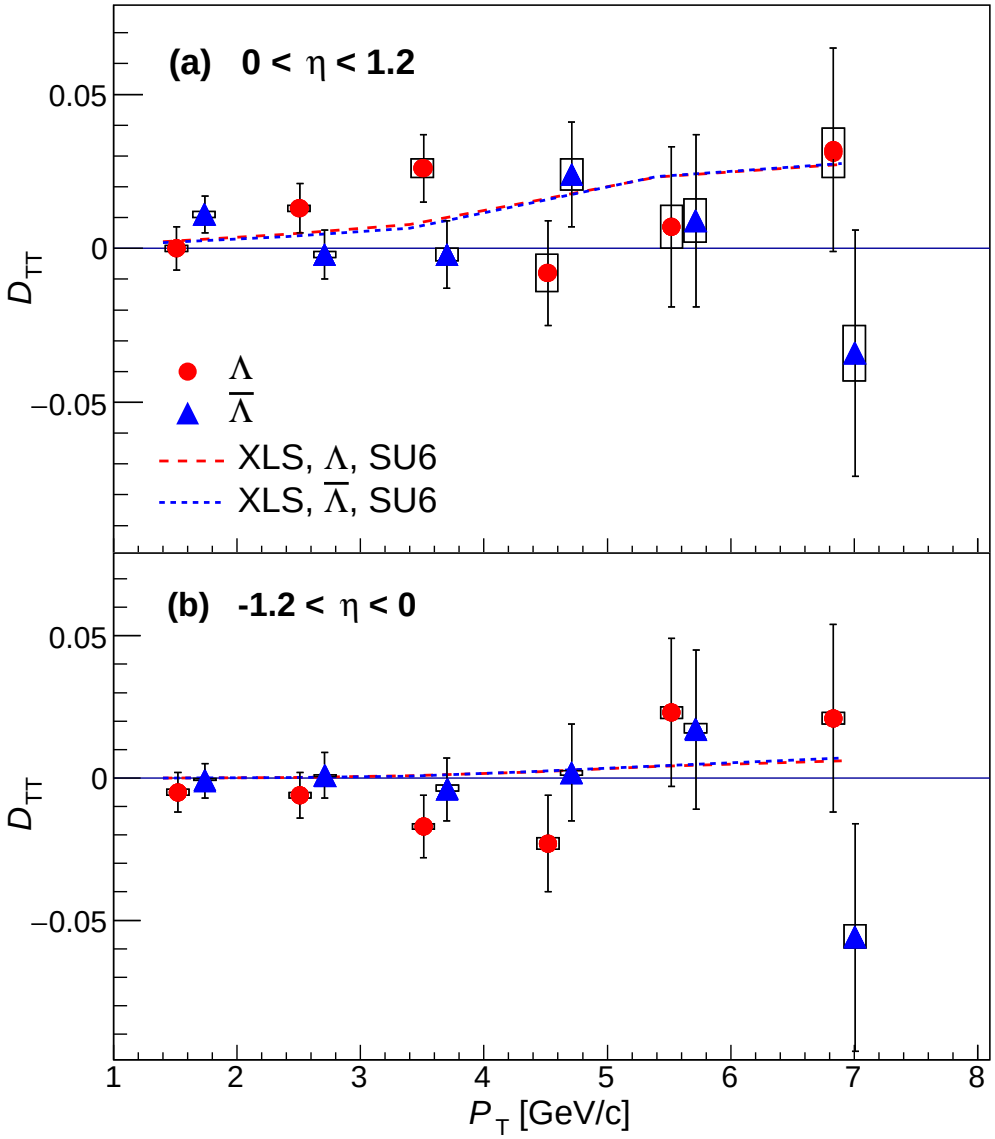

Figure 7.1: D_{TT} extracted from the trigger combined sample for Λ and $\bar{\Lambda}$. The left grpah is with positive η with respect to the polarized beam and the right one is with negative η with respect to the polarized beam.

8 Main Code

The top directory for the code is

`pp200trans_2012`

and the more details and updated introduction of the analysis code can be found in CVS directories.

8.1 Data Analysis: from MuDsts to D_{TT}

Currently, the muDst files for run12_200GeV are not available on RCF disk any longer. For test, one can always download a samll number of muDst files from HPSS. The full file list can be accessed via catalog:

```
get_file_list.pl -keys path,filename \\
-cond production=P12id,trgsetupname~pp200_production_2012, \\
filetype=daq_reco_MuDst,filename~st_physics,\\
tpx=1,emc=1,eemc=1,sanity=1,storage=hpss -limit 0
```

For reading the MuDst files (when the data is on the disk), you can just go inside directory LamRec, compile, and run the executable file Run job.csh, after which the analysis jobs will be submitted. The output files – the Lambda trees can be found in the scratch directory.

More detail steps are shown following:

```
In LamRec:
Lambda reconstruction from MuDst root files.

1. The code compliled with SL16b Library initially
   but the Library seems to be removed. starpro sholud be OK.
2. Excute the following commands:
   starpro
   cons
   Run_jobs.csh start_runIndex end_runIndex
3. The output files will be stored in the Tree directory.


In JetRec:
Jet Tree are simplified here for Lambda and jet correlation.

1. Retrive origin jet tree from HPSS to JetTree directory.
   The jet tree files are located in:
   /home/jcmei/JetTree_run12/JetRec_Kevin/
2. Make file lists in each one of the runs with the whole path.
   MakeList.csh
```

```
3. Submit jobs to simplify jet trees:
   Run_simpleJet_jobs.csh start_runIndex end_runIndex
4. The output files will be stored in the simpleJetTree directory.


In JetMatch:
Make the correlation between Lambda and jets.

1. Make file list.
   makeList.csh
2. Submit jobs to make the correlation.
   Run_job.csh start_runIndex end_runIndex
3. Obtain root files by run.
   mergeBYrun.csh
4. cd dataBYrun
   lss | grep root > file.lis


In Ana directory:
The data is further selected and dealed with to obtain the final results.

1. Go to Select
2. Run_jobs.csh
3. cd data
   lss | grep root > file.lis

4. Go to fillHist
5. Run_job.csh

6. Go to imFit/code/
7. invariant mass fit and background estimetion
   excute_imFit.C

8. To Ana/fiilHist
   Run_job_2cos.csh
9. cd data/cos
   cd sig
   hadd merged_ALL.cos.root ALL/*_ALL.cos.root
   cd ../bkg
   hadd merged_ALL.cos.root ALL/*_ALL.cos.root

10.Extract D_TT
   To Ana/result
```

```
   cos2dtt_crossRatio.csh
   textDtt.csh

11.Make Money plots
   To Ana/imFit/code

   python paperPlot_im.py
   python paperPlot_imcos.py
   python paperPlot_dttcos.py
   python paperPlot_result.py

   The plots will be in the output directory.
```

8.2 MC production

Generation MC data sample:

```
cd mcProduction/Gen/
Run_gen.csh par1 par2 par3
```

Here par1, par2 and par3 are the low and high edges of the hard pT and the circle number of the generation.
Jets and Hyperons reconstruction of MC data sample:

```
cd pp200trans_2012/mcProduction/Rec/
Run_job.csh
```

PTV(hyperon pT) and PTH(hard pT) are needed to specify in the macro.
Make histograms of MC data sample:

```
cd pp200trans_2012/mcProduction/Ana/
cd merge
Run_job.csh

cd ../toHist
Run_job.csh
```

PTV(hyperon pT) and PTH(hard pT) are also needed to specify in the macro.

8.3 Notes

As usual, the .csh and .xml scripts should be appropriately modified as needed (path and directory) and corresponding file lists are needed in some steps. In the code collection directory, the README file should be more updated. Now, all the needed histograms are produced. The trigger bias can be extracted by using a few short macros. In

```
pp200trans_2012/mcProduction/tBias
```

directory, the macros used in this analysis can be taken as reference. Overall, this codes mentioned in this section are not professional enough. If any confusion are met, please feel free to contact Jincheng Mei (jcmei@rcf.rhic.bnl.gov).

A Run List

Here is the run list we used in the final results:

13044126 13045001 13045005 13045006 13045007 13045012 13045029 13045056
13045133 13045134 13045135 13045138 13045145 13045146 13045164 13046001
13046003 13046004 13046121 13047003 13047023 13047024 13047026 13047027
13047028 13047029 13047030 13047031 13047032 13047034 13047035 13047122
13047123 13047124 13047126 13048009 13048010 13048011 13048012 13048013
13048014 13048015 13048016 13048017 13048018 13048019 13048030 13048031
13048032 13048040 13048041 13048042 13048043 13048044 13048045 13048049
13048050 13048051 13048052 13048053 13048087 13048088 13048089 13048090
13048091 13048092 13048093 13049004 13049005 13049006 13049031 13049032
13049035 13049039 13049041 13049042 13049045 13049046 13049047 13049048
13049049 13049050 13049072 13049073 13049080 13049081 13049082 13049086
13049087 13049088 13049093 13049094 13049096 13049098 13049099 13049101
13050001 13050006 13050007 13050009 13050011 13050012 13050016 13050020
13050022 13050023 13050028 13050029 13050031 13050032 13050033 13050036
13050037 13050038 13050039 13050041 13050042 13050043 13050044 13050046
13050047 13051006 13051007 13051008 13051009 13051010 13051011 13051012
13051015 13051016 13051017 13051019 13051020 13051021 13051022 13051023
13051024 13051026 13051028 13051068 13051069 13051070 13051071 13051072
13051073 13051074 13051081 13051083 13051085 13051086 13051087 13051088
13051092 13051093 13051095 13052001 13052002 13052003 13052004 13052005
13052009 13052010 13052011 13052012 13052013 13052014 13052015 13052016
13052017 13052018 13052019 13052020 13052021 13052036 13052037 13052039
13052042 13052043 13052045 13052048 13052050 13052051 13052052 13052053
13052054 13052056 13052061 13052088 13053004 13053005 13053006 13053007
13053012 13053013 13053015 13053027 13053028 13054023 13054044 13054060
13054061 13054062 13054063 13054064 13054065 13054066 13054068 13054069
13054070 13054084 13054085 13055001 13055004 13055006 13055007 13055008
13055009 13055010 13055011 13055014 13055016 13055017 13055018 13055019
13055020 13055021 13055022 13055023 13055024 13055035 13055036 13055037
13055038 13055039 13055068 13055070 13055072 13055073 13055075 13055076
13055080 13055081 13055082 13055086 13055087 13056005 13056007 13056008
13056020 13056021 13056022 13056023 13056024 13056025 13056026 13056027
13056028 13056029 13056030 13056031 13056033 13056034 13056035 13056037
13056038 13056039 13057005 13057006 13057007 13057008 13057009 13057010
13057011 13057014 13057015 13057016 13057017 13057018 13057019 13057021
13057022 13057023 13057024 13057025 13057026 13057027 13057044 13057045
13057046 13057047 13057048 13057049 13057050 13057051 13057052 13057053
13057055 13057056 13057057 13057058 13058002 13058008 13058015 13058016
13058017 13058018 13058025 13058026 13058028 13058029 13058031 13058032

13059005	13059006	13059007	13059008	13059009	13059010	13059011	13059012
13059013	13059014	13059015	13059016	13059017	13059018	13059020	13059021
13059022	13059023	13059025	13059026	13059027	13059076	13059077	13059078
13059079	13059080	13059082	13059083	13059084	13059085	13059086	13059087
13060001	13060002	13060003	13060008	13060009	13060010	13060011	13060012
13061024	13061025	13061029	13061030	13061031	13061035	13061061	13062001
13062002	13062004	13062005	13062006	13062007	13062013	13062025	13062026
13062028	13062029	13062049	13062050	13062052	13062059	13062060	13062061
13062062	13062063	13063009	13063010	13063011	13063020	13063022	13063023
13063030	13063031	13063032	13063034	13063035	13063036	13063053	13063054
13063062	13063063	13063065	13063067	13063068	13063071	13063072	13063073
13063074	13063076	13064001	13064002	13064003	13064004	13064005	13064006
13064012	13064014	13064020	13064021	13064022	13064023	13064024	13064025
13064026	13064028	13064029	13064031	13064032	13064052	13064055	13064056
13064057	13064059	13064061	13064064	13064065	13064066	13064068	13064070
13064074	13064075	13065005	13065006	13065007	13065008	13065009	13065013
13065014	13065015	13065016	13065017	13065018	13065019	13065020	13065021
13065022	13065046	13065047	13065048	13065049	13065050	13065052	13065053
13065055	13065056	13065058	13065059	13065060	13066021	13066022	13066023
13066024	13066025	13066026	13066027	13066028	13066029	13066030	13066031
13066033	13066034	13066035	13066036	13067003	13067010	13067011	13067012
13067013	13068017	13068022	13068027	13068029	13068034	13068036	13068037
13068084	13068085	13068086	13068087	13068088	13068090	13069001	13069002
13069003	13069004	13069005	13069006	13069007	13069008	13069013	13069014
13069016	13069017	13069018	13069020	13069021	13069022	13069023	13069024
13069026	13069027	13069030	13069031	13069035	13069036	13069066	13069067
13069068	13069069	13069073	13070006	13070008	13070010	13070011	13070012
13070014	13070016	13070017	13070018	13070020	13070021	13070022	13070024
13070025	13070026	13070027	13070056	13070057	13070058	13070059	13070060
13070061	13071003	13071004	13071005	13071006	13071008	13071009	13071010
13071011	13071012	13071064	13072001	13072002	13072003	13072004	13072005
13072006	13072007	13072008	13072009	13072010	13072011	13072014	13072015
13072016	13072017	13072018	13072019	13072020			

References

[1] B. I. Abelev, J. Adams, and M. M. al Aggarwal. Strange particle production in $p+p$ collisions at $\sqrt{s} = 200$ gev. *Phys. Rev. C*, 75:064901, Jun 2007.

[2] A. Bravar et al. Spin transfer in inclusive Lambda0 production by transversely polarized protons at 200-GeV/c. *Phys. Rev. Lett.*, 78:4003–4006, 1997.

[3] John C. Collins, Steve F. Heppelmann, and Glenn A. Ladinsky. Measuring transversity densities in singly polarized hadron-hadron and lepton-hadron collisions. *Nuclear Physics B*, 420(3):565 – 582, 1994.

[4] J. Beringer et al. Review of particle physics. *Phys. Rev. D*, 86:010001, Jul 2012.

[5] B. I. Abelev et al. (STAR Collaboration). Longitudinal spin transfer to Λ and $\overline{\Lambda}$ hyperons in polarized proton-proton collisions at $\sqrt{s} = 200$ GeV. *Phys. Rev. D*, 80:111102, Dec 2009.

[6] Torbjorn Sjostrand, Stephen Mrenna, and Peter Z. Skands. PYTHIA 6.4 Physics and Manual. *JHEP*, 05:026, 2006.

[7] Peter Z. Skands. Tuning monte carlo generators: The perugia tunes. *Phys. Rev. D*, 82:074018, Oct 2010.

[8] Qing-hua Xu, Zuo-tang Liang, and Ernst Sichtermann. Anti-lambda polarization in high energy pp collisions with polarized beams. *Phys. Rev. D*, 73:077503, Apr 2006.